

Computation of Incompressible and Weakly-Compressible Viscoelastic Liquids Flow: finite element/volume schemes

M. F. Webster ^{*}, I. J. Keshtiban, and F. Belblidia

Institute of Non-Newtonian Fluid Mechanics,
Department of Computer Science,
University of Wales, Swansea, SA2 8PP, UK.

^{*} Author for correspondence. *Email:* m.f.webster@swansea.ac.uk

Abstract

In this study, we analyse viscoelastic numerical solution for an Oldroyd-B model under incompressible and weakly-compressible liquid flow conditions. We consider flow through a planar four-to-one contraction, as a standard benchmark, throughout a range of Weissenberg numbers up to critical levels. At the same time, inertial and creeping flow settings are also addressed.

Within our scheme, we compare and contrast, two forms of stress discretisation, both embedded within a high-order pressure-correction time-marching formulation based on triangles. This encompasses a parent-cell finite element/SUPG scheme, with quadratic stress interpolation and recovery of velocity gradients. The second scheme involves a sub-cell finite volume implementation, a hybrid *fe/fv* scheme for the full system.

A new feature of this study is that both numerical configurations are able to accommodate incompressible, and low to vanishing Mach number compressible liquid flows. This is of some interest within industrial application areas. We are able to provide parity between the numerical solutions across schemes for any given flow setting. Close examination of flow patterns and vortex trends indicates the broad differences anticipated between incompressible and weakly-compressible solutions. Vortex reduction with increasing Weissenberg number is a common feature throughout. Compressible solutions provide larger vortices (salient and lip) than their incompressible counterparts, and larger stress patterns in the re-entrant corner neighbourhood. Inertia tends to reduce such phenomena in all instances. The hybrid *fe/fv*-scheme proves more robust, in that it captures the stress singularity more tightly than the *fe*-form at comparable Weissenberg numbers, reaching higher critical levels. The sub-cell structure, the handling of cross-stream numerical diffusion, and corner discontinuity capturing features of the hybrid *fe/fv*-scheme, are all perceived as attractive additional benefits that give preference to this choice of scheme.

KEY WORDS: Compressible liquid flow, high-order pressure-correction, low Mach number, Oldroyd-B, planar contraction, critical Weissenberg number, vortex behaviour

1. Introduction

In our previous studies [14,34], we have developed a numerical scheme for Newtonian and viscoelastic weakly-compressible liquid flows based on a pure finite element (*fe*) methodology. There, we demonstrated the capability of this method to deal with complex flows. In this article, we introduce a hybrid finite element/finite volume (*fe/fv*) algorithm to handle such flows at low Mach number (Ma) and Reynolds number (Re) under isothermal conditions. The finite volume (*fv*) sub-cell scheme is incorporated for the hyperbolic constitutive equation, considered here of Oldroyd-B form. This model provides a constant shear viscosity and strain-hardening (unbounded) properties in extension. The continuity/momentum balance is accommodated through a semi-implicit fractional-staged/pressure-correction *fe*-formulation.

Compressibility effects are characterised by the Mach number, the ratio of the speed of fluid flow (u) to the speed of sound (c). The incompressible limit of a compressible flow is obtained, under suitable constraints on length and time scales, when the Mach number asymptotes to zero ($Ma \approx 0$) [21]. Low Mach number (LMN) flows may arise for either liquid or gas material states, with dependency on physical conditions. Liquid materials are frequently considered as incompressible, as density tends to reflect a weak functional dependence upon pressure. Therefore, such flows may reflect the influence of compressibility under exposure to high pressure-differences, particularly for highly viscous/viscoelastic materials, or in instances such as liquid impact or jet cutting.

LMN flow computations remain a significant challenge, notwithstanding the success of some compressible flow solvers in simulating many complex compressible flows. Many numerical methods encounter severe difficulties when dealing with instances where $Ma < 0.3$ [35], where deterioration of efficiency and accuracy are experienced. One of the key difficulties arises from the fact that the governing equation system switches in type. The equations for viscous compressible flow form a hyperbolic-parabolic system of finite wave-speeds (inviscid case, hyperbolic), whilst those for incompressible viscous flow assume an elliptic-parabolic system with infinite propagation rates. This is augmented for viscoelastic flows by a sub-system of hyperbolic form. The lack of efficiency in solving the compressible equations for LMN is associated with large disparity in wave speeds across the system [35], see Appendix for more detail.

There is significant interest in developing numerical algorithms to deal with LMN flows for viscoelastic liquid flows, where Ma approaches zero. LMN flows adopt an important role in nature and industrial processing. In many technical applications, liquid flow can demonstrate significant compressibility effects. This would include examples of: injection molding, high-speed extrusion, jet cutting, liquid impact, and under recovery of and

exploration for petroleum. Under such circumstances, the compressibility of viscoelastic liquids should be taken into account, in order to accommodate typical flow phenomena arising, say cavitation [6] or flow instabilities [10]. In capillary rheometry, compressibility effects may be significant and have a major impact upon the time-dependent pressure changes in the system [17]. If numerical simulations are to prove accurate, such physics must be accounted for.

There are two major computational approaches adopted to solve LMN flows: pressure-based methods (incompressible solvers) and density-based methods (compressible solvers). With *pressure-based methods* pressure is a primitive variable and density a dependent variable. The first implementation of pressure-based schemes for compressible LMN flows may be attributed to Harlow and Amsden [12]. The use of pressure as a primary variable allows computation to remain tractable over the entire spectrum of Mach numbers. This is due to the fact that pressure changes remain finite, irrespective of prevailing Mach Number [13]. Moreover, extension of these method to compressible flows retains robustness [21]. On the other hand, with *density-based methods*, continuity provides an equation for density, and pressure is obtained from an equation of state. In pressure-based methods, continuity is utilized as a constraint on velocity and is combined with momentum to form a Poisson-like equation for pressure. These two approaches are quite different, with respect to their choice of variables, sensitivity to numerical stability and choice of solvers [19]. Since our constructive formalism emanates from incompressible flow, it is natural for us to consider pressure-based methods. In addition, the vast majority of incompressible viscoelastic schemes are pressure-based, and on such grounds, may be preferred for algorithmic development.

In the fe-context, based on the ideas of Van Kan [31], Townsend and Webster [28] introduced a second-order Taylor-Galerkin/pressure-correction (TGPC) scheme. This fractional-staged formulation introduced an operator-splitting stencil of predictor-corrector structure, significantly reducing computational overheads. In this manner, solutions have been derived previously for incompressible viscoelastic flows [7,18]. Under the TGPC scheme, *fe*-treatment of the constitutive equations incorporates consistency through Taylor-Petrov-Galerkin streamline upwinding (TSUPG), with recovery applied upon velocity gradients [18].

In the fv-context, Webster and co-workers [1-3] have advanced an alternative spatial discretisation, via a novel hybrid *fe/fv*-scheme for steady incompressible viscoelastic flows. With this methodology, the constitutive equation is accommodated via a sub-cell cell-vertex *fv*-algorithm. The main philosophy here is to apply *fe*-stencils to the self-adjoint component of the system, and *fv*-forms to the hyperbolic sections. The above studies are concerned with incompressible flow considerations.

With compressible flow in mind, Webster and co-workers [14,34] have already provided extension to the ‘pure *fe*’ TGPC algorithm, handling weakly-compressible viscos-

viscoelastic liquid flows at LMN, termed C-TGPC (Compressible-TGPC). Under such setting, the divergence-free condition applicable for incompressible flow, is replaced with the continuity equation for compressible liquid flow. The temporal derivative of density is interpreted through pressure representation, via an equation of state. For this purpose, two discrete representations have been proposed to interpolate density: a piecewise-constant form with gradient recovery and a linear interpolation form, similar to that on pressure. Both density interpolations provide identical solutions. The piecewise-constant interpolation scheme is selected for its advantages of order retention and efficiency in implementation. Previously, this pure *fe*-implementation has been successfully tested on a number of standard benchmark problems. Consistency has been realised in simulating compressible flows ($Ma < 0.3$), as well as almost incompressible liquid flows ($Ma \approx 0$). As such, enhanced convergence properties have been gathered compared to the original TGPC algorithm. In addition, in the present study we are interested in advancing the hybrid formulation, via embedding compressibility considerations, leading to a compressible hybrid *fe/fv*-implementation.

The present article is organized as follows: the governing equations for compressible viscoelastic flow are expounded in Section 2. In Section 3, we introduce the fractional equation stages of the viscoelastic pressure-correction scheme, outlining the spatial discretization strategies employed as necessary. In Section 4, we present the application of our methodology to the 4:1 contraction flow test-problem. A continuation solution strategy, through increasing Weissenberg number (We), is adopted in seeking steady-state solutions. Throughout the study, we conduct comparison across scheme variants and flow settings, drawing upon the literature. The schemes proposed are validated for consistency and accuracy at a fixed level of $We=1.5$. This is followed by analysis up to critical levels of Weissenberg number. Differences due to inclusion of compressibility effects and inertia are highlighted through flow patterns and vortex activity.

2. Governing equations

For compressible viscoelastic flow, the governing non-dimensional equations for conservation of mass, momentum, and the development of stress may be expressed as:

$$\frac{\partial \rho}{\partial t} + \nabla \cdot (\rho u) = 0, \quad (1)$$

$$\text{Re } \rho \frac{\partial u}{\partial t} = \nabla \cdot \left(2 \frac{\mu_s}{\mu} d + \tau \right) - \text{Re } \rho u \cdot \nabla u - \nabla p. \quad (2)$$

The constitutive state law for an Oldroyd-B model fluid is expounded, viz.

$$We \frac{\partial \tau}{\partial t} = -Weu \cdot \nabla \tau + We(L \cdot \tau + \tau \cdot L^T) + 2 \frac{\mu_e}{\mu} - \tau. \quad (3)$$

Here, ρ, u, p, τ represent fluid density, velocity vector, pressure and extra-stress tensor respectively; $d_{ij} = (L_{ij} + L_{ij}^T)/2 - L_{ij}^T \delta_{ij}/3$ represents an augmented rate-of-deformation tensor and $L^T = \nabla u$, the velocity gradient. The total viscosity, μ splits into Newtonian (solvent) viscosity, μ_s , and elastic (polymeric), μ_e , components, such that $\mu = \mu_e + \mu_s$. Here, we take $\mu_s/\mu = 1/9$. Non-dimensional group numbers, of Reynolds and Weissenberg numbers, are defined as:

$$Re = \frac{\rho UL^o}{\mu}, \quad We_e = \frac{\lambda U}{L^o} \quad (4)$$

where, λ is a relaxation time, U a characteristic velocity (averaged at outlet) and L^o is a length-scale (channel-exit half-width). To complete the set of governing equation, it is necessary to introduce an equation of state to relate density to pressure. Here, we employ the modified Tait equation of state [27], a well-established formulation for liquids,

$$\frac{\tilde{p} + B}{\tilde{\rho}_0 + B} = \left(\frac{\rho}{\rho_0} \right)^m, \quad \text{with augmented pressure } \tilde{p} = p - \frac{1}{3} \text{trace} \left(\tau + 2 \frac{\mu_s}{\mu} d \right). \quad (5)$$

Parameters B and m are constants[†], and $\tilde{\rho}_0, \rho_0$ denote reference scales for pressure and density. Assuming isentropic conditions (see [13]), and employing the differential chain rule, we gather,

$$\frac{\partial \rho}{\partial t} = \frac{\partial \rho}{\partial p} \frac{\partial p}{\partial t} = \frac{1}{c_{(x,t)}^2} \frac{\partial p}{\partial t}, \quad (6)$$

$$\frac{\partial p}{\partial \rho} = \frac{m(\tilde{P} + B)}{\rho} = c_{(x,t)}^2, \quad (7)$$

where, $c_{(x,t)}$ introduces the speed of sound, a field variable, distributed in space and time.

3. Numerical Discretisation

The C-TGPC scheme is a time-stepping procedure of multiple fractional-staged equations. The pressure-correction procedure accommodates the continuity constraint to second-order accuracy in time, introducing a three-staged structure per time-step cycle (see [28,30]). At stage one, a predictor-corrector equation doublet, provides velocity and stress fields, predicted at the half time-step $(u, \tau)^{n+\frac{1}{2}}$ and corrected for the full time-step $(u^*, \tau)^{n+1}$. The momentum

[†] Generally, B and m are functions of temperature.

diffusion term is treated in a semi-implicit manner to improve stability and convergence properties. The velocity field (u^*), derived over the full time-step for momentum, may not satisfy continuity, and necessitate correction. This generates a Poisson-like equation for the time-step increment of pressure (stage 2), accompanied with a correction stage (stage 3). Departure from the incompressible implementation, to incorporate compressible representation, is principally identified at stage 2.

Step 1a (prediction):

$$\frac{2\text{Re}\rho^n}{\Delta t} \left(u^{n+\frac{1}{2}} - u^n \right) = \left[\nabla \cdot \left(2 \frac{\mu_s}{\mu} d^n + \tau \right) - \text{Re} \rho u \cdot \nabla u - \nabla p \right]^n + \nabla \cdot \frac{\mu_s}{\mu} \left(d^{n+\frac{1}{2}} - d^n \right), \quad (8)$$

$$\frac{2\text{We}}{\Delta t} \left(\tau^{n+\frac{1}{2}} - \tau^n \right) = \left[2 \frac{\mu_e}{\mu} d - \tau - \text{We} \{ u \cdot \nabla \tau - L \cdot \tau + \tau \cdot L^T \} \right]^n, \quad (9)$$

Step 1b (correction):

$$\frac{\text{Re}\rho^n}{\Delta t} (u^* - u^n) = \left[\nabla \cdot \tau - \text{Re} \rho u \cdot \nabla u \right]^{n+\frac{1}{2}} + \left[\nabla \cdot 2 \frac{\mu_s}{\mu} d - \nabla p \right]^n + \nabla \cdot \frac{\mu_s}{\mu} (d^* - d^n), \quad (10)$$

$$\frac{\text{We}}{\Delta t} (\tau^{n+1} - \tau^n) = \left[2 \frac{\mu_e}{\mu} d - \tau - \text{We} \{ u \cdot \nabla \tau - L \cdot \tau + \tau \cdot L^T \} \right]^{n+\frac{1}{2}}. \quad (11)$$

The pressure field is obtained through *stage 2*,

$$\frac{1}{\Delta t c_{(x,t)}^2} (p^{n+1} - p^n) - \Delta t \theta \nabla^2 (p^{n+1} - p^n) = -\rho^n \nabla \cdot u^* - u^* \cdot \nabla \rho^n, \quad (12)$$

and finally, the velocity is corrected to satisfy continuity at *stage 3*,

$$\frac{\text{Re}\rho^{n+1}}{\Delta t} (u^{n+1} - u^*) = -\theta \nabla (p^{n+1} - p^n). \quad (13)$$

The *fv*-tessellation is constructed from the *fe*-grid by connecting the mid-side nodes. This generates four triangular *fv*-sub-cells per *fe*-parent cell, as demonstrated in Figure 1a. Stress variables are located at the vertices of *fv*-sub-cells. In contrast, quadratic velocity interpolation is enforced on the parent *fe*-cell, alongside linear pressure interpolation. The constitutive equation displays hyperbolic character, via the Oldroyd-B model. Therefore, for effective numerical discretisation, it is necessary to employ particular upwinding treatment. Note, in viscoelastic flows for high *We*, the elastic stress component may be large in contrast to its viscous counterpart. In addition, there is viscous diffusion present, which may dissipate instability, and through which fluctuations may arise from inaccurate representation of

advection. No such operator is present in the constitutive equation, and therefore at high- We , accuracy in upwind modelling for elastic contributions, has crucial influence on scheme behaviour. This may prove a source of numerical instability, stimulated by large values of velocity, elastic stress, and/or their gradients. For some methods (for example, EVSS), operator-splitting artificially introduces some ellipticity into the problem via the constitutive equation (see also, earlier approaches of EMEE-type [16]) . This has the effect of damping some of the numerical noise generated, yet adjusts the physics of the problem at the same time.

Different stress upwinding techniques are incorporated into the above framework within fe and fv -methods. Within the fe -scheme, a Taylor-Petrov-Galerkin procedure, with recovery for velocity gradients is utilised. For the sub-cell fe/fv -scheme, a cell-vertex fv -scheme, based on fluctuation distribution (FD) ideology, has been employed. Originally, such upwinding schemes were designed for pure-convection problems. These FD schemes possess properties such as conservation, linearity preservation and/or positivity. Briefly, one can recast stress equations, via the flux (R) and source terms (Q). For the Oldroyd-B model, this can be expressed as follows:

$$\frac{\partial \tau}{\partial t} = -R + Q, \quad (14)$$

$$R = u \cdot \nabla \tau, \quad (15)$$

$$Q = \frac{1}{W_e} \left(2 \frac{\mu_e}{\mu} - \tau \right) + L \cdot \tau + \tau \cdot L^T. \quad (16)$$

Each scalar component of stress tensor, τ acting on an arbitrary volume, whose variation is controlled through the fluctuation of the flux vector ($R = u \cdot \nabla \tau$) and the scalar source term (Q),

$$\frac{\partial}{\partial t} \int_{\hat{\Omega}_l^T} \tau d\Omega = \int_{\hat{\Omega}_l^T} R d\Omega + \int_{\hat{\Omega}_l^T} Q d\Omega. \quad (17)$$

In the above expression, integrals are evaluated over two different control volumes: the sub-cell triangle T and median-dual-cell control volume (l) (see Figure 1c). The core of this cell-vertex fluctuation distribution scheme is to evaluate these flux and source terms on each fv -triangle. The update for a given node (l) is obtained by summing the contributions from control volume, $\hat{\Omega}_l$, that is composed of all fv -triangles surrounding node l , see Figure 1c. It is more convenient to treat the flux and source terms separately, as each may have different propagation mechanisms. One may write the above integrals for a particular triangle T in the form:

$$\hat{\Omega}_l^T \frac{\tau_l^{n+1} - \tau_l^n}{\Delta t} = \alpha_l^T R_T + Q_{MDC_T}^l, \quad (18)$$

where, $\hat{\Omega}_l^T$ is the area of the median dual cell (MDC_T) associated with node (l) within the triangle T . To accommodate upwinding, the flux term R_T is calculated over triangle T , and is distributed over the vertex nodes based on flow direction and coefficients α . Here, for node (l), α_l^T designates the contribution to node (l) from flux R_T on triangle T . A key feature of the cell-vertex fv -method lies within the definition of α -coefficients. Webster and co-workers [2,3] found the Low Diffusion B (LDB) scheme appropriate, for steady viscoelastic flows where source terms may dominate. This is a linear scheme with linearly preservation properties and second-order accuracy [3]. It conveys a relatively low-level of numerical diffusion in comparison to a linear positive scheme. The LDB distribution coefficients α_i are obtained on each triangle via angles γ_1, γ_2 (see Figure 1b), subtended at an inflow vertex (i) by the advection velocity \mathbf{a} (average of velocity field per fv -cell), viz.

$$\alpha_i = \frac{\sin \gamma_1 \cos \gamma_2}{\sin(\gamma_1 + \gamma_2)}, \quad \alpha_j = \frac{\sin \gamma_2 \cos \gamma_1}{\sin(\gamma_1 + \gamma_2)}, \quad \alpha_k = 0. \quad (19)$$

Note, when γ_1 is larger than γ_2 , then α_i is larger than α_j , and hence by design, node (i) gains a larger contribution from the flux than node (j).

The flux R_T and the source Q_{MDC}^l terms, as evaluated in Eq.(18) over different control volumes, create some inconsistency introducing inaccuracy even for simple model problems. To rectify this position, Wapperom and Webster [32] proposed a generalised formulation that consistently distributes both flux and source terms over the fv -triangle, viz.,

$$\frac{\hat{\Omega}_l^T (\tau_l^{n+1} - \tau_l^n)}{\Delta t} = \delta_T \alpha_l^T (R_T + Q_T) + \delta_{MDC_T} (R_{MDC_T}^l + Q_{MDC_T}^l). \quad (19)$$

The parameters δ_T and δ_{MDC} are applied to discriminate between various update strategies, being functions of fluid elasticity, velocity field and mesh size. By appropriate selection of δ_T and δ_{MDC} , one can obtain various blends for different flow regimes. With $\delta_T = f(We, a, h)$ and $\delta_{MDC} = 1$, the nodal update is similar to consistent streamline upwinding, as used in fe -schemes. We follow [2,3,32] such that $\delta_{MDC} = 1$ and $\delta_T = \xi/3$, if $|\xi| \leq 3$ and 1 otherwise. Here, $\xi = We_e(a/h)$, with a the magnitude of the advection velocity, averaged per fv -cell and h is a mesh-size scale (square-root of the fv -cell size). Subsequently,

Aboubacar [1-3] proposed a method with appropriate area weighting to enforce time consistency,

$$\frac{(\tau_l^{n+1} - \tau_l^n)}{\Delta t} = \frac{\sum_{\forall T} \delta_T \alpha_l^T (R_T + Q_T)}{\Omega_{FD}} + \frac{\sum_{\forall T} \delta_{MDC_T} (R_{MDC_T}^l + Q_{MDC_T}^l)}{\Omega_{MDC}}, \quad (20)$$

where, $\Omega_{FD} = \sum_{T_l} \delta_T \alpha_l^T \Omega_T$ and $\Omega_{MDC} = \sum_{MDC_l} \delta_{MDC_T} \Omega_l^T$.

4. Discussion of results

Flow through an abrupt contraction for an Oldroyd-B fluid is well-documented in the literature, where it is recognised as a valuable benchmark problem, useful to qualify numerical stability of schemes at high We -levels. It is a natural choice in this study for two principal reasons. First, from a numerical point of view, it presents a relatively simple geometric configuration, generating complex shear and extensional deformation, allowing a framework to investigate numerical schemes for complex viscoelastic flows. Second, from a practical standpoint, its relevance arises in several polymeric processing applications, such as in injection molding, extrusion and rheometry itself.

4.1. Literature review

A challenging feature of the abrupt contraction (non-smooth) flow problem is the presence of a stress singularity at the re-entrant corner, which impacts upon stability properties of numerical schemes. Many fluid models suffer a limiting Weissenberg number (We), beyond which numerical solutions fail. This issue has become known as ‘the high We problem-HWNP’ [15], drawing considerable attention over the last two decades or so. In *the incompressible context*, and commenting upon our own contributions, one may site those based on the ‘pure’ fe -framework, from Carew *et al.*, [7] and Matallah *et al.*, [18], providing literature reviews and consensus findings on vortex behaviour. Subsequently, Wapperom and Webster [32] introduced a hybrid fe/fv -methodology. This was developed further in Aboubacar and Webster [1]. There, mesh refinement was conducted for an Oldroyd-B model. Extension of this work in Aboubacar *et al.*, [2,3], focused on alternative geometries (planar and axisymmetric, sharp- and rounded-corners) and several viscoelastic models (Oldroyd-B and PTT-variants). An overview of experimental and numerical studies was also documented there.

Elsewhere, Guénette and Fortin [11] proposed a stable and cost-effective mixed fe -method, a variant of the EVSS formulation. Numerical results were presented for the PTT fluid model. Yurun [37] compared two variants of EVSS fe -schemes on this benchmark problem (discontinuous Galerkin DG and continuous SUPG). The DG/EVSS scheme was observed to reflect significant improvement over the SUPG/EVSS variant at higher We -levels

(smoothness in solutions and enhanced robustness, see on for fv -solutions). The above subject matter is covered in the comprehensive literature review of Baaijens [5].

In *the context of fv -formulations*, Phillips and Williams [23,24] investigated the differences in vortex structure and development, with and without inertia. This work covered planar and axisymmetrical configurations, and was based on a semi-Lagrangian fv -method. Similarly, Mompean [20] proposed an approximate algebraic-extra-stress fluid model, via a second-order fv -scheme, employing a staggered-grid technique. Likewise, Alves *et al.*, [4] invoked an extremely refined mesh to chart in detail the development of both vortex-size and intensity for Oldroyd-B and PTT fluids. Similarly to Aboubacar *et al.*, [2,3] their work[†] highlighted that, suitable mesh refinement is necessary in the re-entrant corner zone to sharply capture the singularity there. This often reduces the critical level of We (We_{crit}) attained, when compared to that gained on poorer quality meshes. Predominantly, the above cited studies are restricted to steady-state solutions and the incompressible flow domain.

Under *compressible liquid flow considerations*, earlier Keshtiban *et al.*, [14] have extended an incompressible viscoelastic fe -scheme to handle weakly-compressible flows. The emerging new scheme has been validated on several benchmark problems, including that of present interest of an abrupt four-to-one contraction flow. Over its incompressible counterpart, no loss of accuracy was observed, and convergence properties were enhanced, in seeking steady-state solutions.

4.2. Problem specification

We compare and contrast the compressible fe and hybrid fe/fv -volume schemes, focusing on the sharp-corner 4:1 planar contraction flow, shown schematically in Figure 2a. The total channel length is taken as 76.5 units. We take advantage of flow symmetry about the horizontal central axis running through the domain, thereby computing solutions on half the problem domain. No-slip boundary conditions are adopted on solid walls. At the inlet, transient boundary conditions are imposed reflecting build-up through flow-rate (Waters and King [33]). This generates set transient profiles for normal velocity (U) and stress (τ_{xx} , τ_{xy}), and displays vanishing cross-sectional velocity (V) and stress (τ_{yy}). This procedure improves numerical stability, in convergence to steady-state, providing smooth growth in driving boundary conditions at any particular We , and moreover, introduces true transient features to the computation, see Carew *et al.*, [7] for further details. Over the exit-zone, weak-form natural boundary conditions are established, via boundary integrals within the momentum equation representation under vanishing cross-stream velocity. A pressure reference level is set to zero at the outlet. Throughout compressible flow computations, the Tait parameter set,

[†] Ellipticity, via diffusion smoothing, was introduced into the stress equation.

$(m,B)=(4,10^2)$, is selected, leading to a maxima in doublet $(Ma,\rho)\approx(0.1,1.3)$. Variation in density is noted above the constant incompressible level of about 30%. This level is somewhat purposefully exaggerated to highlight the effects of compressibility within the liquid and the flexibility of the numerical scheme to deal with such compressibility settings. In addition, to represent limiting incompressible conditions $((Ma,\rho)\approx(5*10^{-5},1.0))$, a Tait parameter pairing, $(m,B)=(10^4,10^5)$, is utilised. By selecting this larger Tait parameter pairing, the consistency of the compressible scheme may be investigated[†]. In this case, the incompressible regime may be approached in the limit of vanishing Ma , allowing for comparison of compressible scheme solutions ($Ma\approx 0$) against those for their ‘purely’ incompressible counterparts ($Ma=0.0$). Both creeping ($Re=0.0$) and inertial ($Re=1.0$) flows are considered. In order to capture the numerical singularity affecting the re-entrant corner zone, a fine mesh of structure M3 in [34] is employed, based on 2987 triangular parent- fe cells, see Figure 2b. A suitable dimensionless time-step is adopted throughout (typically, $O(\Delta t=10^{-4})$), satisfying local Courant number conditions [7]. Convergence to steady-state is monitored, via a relative L_2 increment norm on the solution, taken to a time-stepping termination tolerance of $O(10^{-6})$.

Numerical simulations to steady-state are performed for both fe and hybrid fe/fv -schemes under incompressible ($Ma=0.0$), limiting ($Ma\approx 0$), and weakly-compressible ($Ma=0.1$) settings. To investigate numerical stability and accuracy properties through time-stepping of each variant, we employ a continuation solution strategy through increasing We , to extract steady-state solutions. This procedure is implemented as follows: we commence each simulation at $We=0.1$ from a quiescent state in all field variables. Next, solution is sought incrementing directly to $We=1.0$, commencing from the solution at $We=0.1$. This is followed by successive computations, elevating the We -level incrementally in steps of 0.1, until the selected scheme fails to converge (encountering numerical divergence or oscillatory non-convergence to a unique state).

In presenting our results through field data and profiles, we proceed for each scheme variant through three sub-sections. The first, compares scheme variants at a fixed and moderate We -level (here, $We=1.5$). In the second sub-section, critical We -levels are sought, highlighting numerical stability properties for each individual flow/scheme setting. In the last sub-section, we analyse trends in vortex behaviour, through parameterisation in vortex-size and intensity. Comparison with the literature is quoted throughout. The convention for presentation across schemes is to display corresponding plots for the fe -scheme to the left and the hybrid fe/fv -counterpart to the right of each figure.

[†] This is an important feature in computation of LMN flows, where many compressible flow solvers suffer degradation in consistency as Ma approaches zero.

4.3. Numerical solutions at $We=1.5$ - across scheme variants

First, we commence by investigating consistency and accuracy across numerical schemes (fe and fe/fv) under the three Mach number settings quoted above. For this part of our investigation, we select for comparison purposes the level of $We=1.5$, and neglect inertia. Numerical assessment of scheme variants is made on field variable representation, streamline patterns and stress profiles. For incompressible implementations (fe and fe/fv), under-relaxation (R) is called upon to enhance numerical stability. This relaxation procedure may be interpreted as time-step scaling upon each individual equation-stage (see [14] for detail). Here, we have found it effective to retain a uniform under-relaxation factor of $\beta=0.7$.

Incompressible liquid flow: We provide field solution plots in Figure 3, concentrating on the contraction zone. This data includes pressure (top), stress components τ_{xx} and τ_{xy} (middle), and stream-function (bottom). Note, in all streamline plots, a total of fifteen levels, are dispatched covering core-flow: ten equitable levels, from 1.0 to 0.1, followed by two levels at 0.01 and 0.001; plus four levels to illustrate the salient-corner-vortex (inclusive from a minimum level to the zero, separation-streamline). Similar field contour patterns at equivalent levels are observed for both scheme variants, both with under-relaxation (R) and without relaxation (nR). Only minor discrepancy is noted between schemes; about 0.7% in pressure and 2.6% in stream-function. Solutions are observed to faithfully reproduce those presented elsewhere [3,4,18,24].

Figure 4 quantifies the above via stress profiles, for τ_{xx} (top) and τ_{xy} (bottom), at $y=3.0$ along the downstream boundary-wall (see Figure 2a). For plotting clarity, a shift in the position of the re-entrant corner is introduced in under-relaxed (R)-plots. There are practically no differences detected, with or without under-relaxation. Levels in both stress component (τ_{xx}, τ_{xy})-peaks at the re-entrant corner, are larger for the hybrid fe/fv above the fe -form (by about 1.4 times for τ_{xx} and twice for τ_{xy}). One may attribute this to the deeper interpolation quality of the hybrid form (refinement in mesh through sub-cells). Beyond the re-entrant corner and along the wall, there is no growth of stress, reaching equitable levels independently of the scheme employed. Scheme comparison, provides a level of confidence in the validity of these incompressible solutions.

Weakly-compressible liquid flow: Results are presented for both schemes in a similar fashion to the foregoing, though field variable plots (Figure 5 as Figure 3) and stress profiles (Figure 6 as Figure 4). Additionally, field plots are now provided for density variation (Figure 5b). Note, no under-relaxation is necessary for compressible implementations, as numerical stability is found to be satisfactory without such measures. Oncemore, similar contour patterns at equitable levels are observed for both schemes (discrepancy in pressure is 1%; in density, 0.2%). Conspicuously, density representation, across the channel section

($x=\text{constant}$), declines from the centreline to the wall, due to the relationship between density and pressure, upheld via the Tait equation of state (Eq.(5)). In this instance, τ_{xx} (and hence trace τ) is larger at the wall than the centreline. Note, under Newtonian conditions, density contours mimic those in pressure.

Figure 6 illustrates solution profiles in τ_{xx} (top) and τ_{xy} (bottom), for both schemes at the boundary wall ($y=3.0$). The levels of stress-peak are comparable to those of the incompressible instance of Figure 4, when comparing both fe to fe/fv -solutions. The main differences to observe against incompressible counterparts, lie in the sustained growth in both stress components along the boundary wall. This growth rate is constant, described by its angle. These angles are larger for τ_{xx} (12° for τ_{xx} compared to 4° for τ_{xy}), and reflect independence of the specific spatial discretisation employed. At $We=1.5$, we notice oscillatory patterns, behind the singularity corner, in the fe -stress plots, which disappear in the fe/fv -profiles. This is due to the ability of the fe/fv to deal with sharp solution gradients and superior suppression characteristics on numerical cross-stream diffusion. By design, this is not the case with the SUPG/ fe -implementation, as observed by others [37].

Scheme and flow setting comparison: Quantitative comparison of U-profiles along the centreline ($y=4$, see Figure 2a) is undertaken, in Figure 7. This includes assessment of fe and fe/fv -algorithmic implementations for both incompressible ($Ma=0.0$, Figure 7a) and weakly-compressible ($Ma=0.1$, Figure 7b) variants. In addition, we provide $Ma\approx 0$ limit and incompressible ($Ma=0$) comparison (Figure 7c, fe ; Figure 7d, fe/fv). At this We -level, close agreement is observed between implementations, under these alternative flow configurations. The U-profile remains flat beyond the re-entrant corner plane for incompressible flow, whilst it increases monotonically for compressible flow. This maintains a balance in mass-flow rate (ρU , see Figure 7b) overall, as density at the inlet is some 30% larger than that at the exit. Furthermore, as with stress above and for both schemes, $Ma\approx 0$ solutions lie within less than 0.1% of their incompressible equivalents.

4.4. Increasing We - solution strategy

Here, both fe and fe/fv -solutions are sought under the three Ma -flow settings for increasing We up to critical limiting levels. Initially, liquid inertia is omitted in these calculations.

Incompressible liquid flow

In Figure 8, solution profiles for principal stress N_1 are plotted across each scheme. The effect of introducing under-relaxation (bottom) is also highlighted. We comment upon critical levels of We attained, in passing, recorded for immediate comparison in Table 1.

a) *Without relaxation*: Stress-peaks are larger for the fe/fv -scheme (peak $We_{crit}=3.0$) compared to their fe -counterpart (peak $We_{crit}=2.2$). At the same We -level, say $We=2.0$, there is about 30% increase in the stress-peak for the fe/fv above the fe -form. With the fe/fv -scheme, at $We=2.0$ and above, in a small region beyond the corner, the principal stress-peak is followed by two short duration oscillations, that are rapidly damped away travelling further downstream. Similar oscillatory behaviour has been observed earlier by both Yurun [37] and Phillips and Williams [23].

b) *With under-relaxation*: At $We=2.5$, there is about 12% decrease in the stress-peak for the fe/fv below the fe -variant. In contrast to the non-relaxed results at $We=2.0$, there is barely any difference in stress-peak level with the fe -scheme, whilst there is about 30% reduction with the relaxed fe/fv result. Downstream oscillations are also reduced for the relaxed fe/fv -scheme compared to its non-relaxed form. Overall, under-relaxation enhances scheme stability, when compared to its non-relaxed counterpart. On We_{crit} -levels, with the fe -scheme, there is increase from 2.2 to 2.8; a position matched with the fe/fv -scheme, demonstrating increase from 3.0 to 3.5.

Weakly-compressible flow

Figure 9 illustrates corresponding N_1 -profiles for both $Ma \approx 0$ and $Ma=0.1$ settings (discarding relaxation). Independent of flow scenario and across schemes, stress-peaks for the fe/fv -scheme may amount to some four times larger than those of their fe -counterparts (at $We=1.5$, the fe/fv -stress peak is about 40% larger for $Ma \approx 0$ and double that for $Ma=0.1$ compared to their fe -counterparts). This is mainly due to sub-cell refinement and the particular reduced corner integration technique applied: a discontinuity-capturing treatment for the corner solution-singularity unique to the hybrid scheme [1]. When evaluating unrelaxed compressible $Ma \approx 0$ solutions against their truly incompressible counterparts ($Ma=0$) for the fe -scheme, equitable stress-levels are observed at $We_{crit}=1.5$. This is not the case for the corresponding fe/fv -scheme, as stress-peak levels are somewhat elevated from around 105 units for $Ma=0$, to 180 units for $Ma \approx 0$, see back to Figure 8. These discrepancies we would attribute to the alternative fe/fv -discrete implementation in the corner neighbourhood (as above); and also, to the additional sharp velocity gradient contributions made there within the compressible formulation $(L_{ij}^T \delta_{ij} / 3)$. Under the compressible configuration ($Ma=0.1$), the We_{crit} -level is about twice as large for the fe/fv -implementation (peak $We_{crit}=3.1$), when compared to that for the fe -form (peak $We_{crit}=1.7$). Nevertheless, when comparing compressible, $Ma \approx 0$, We_{crit} -levels against their incompressible counterparts the compressible fe -scheme implementation reduces We_{crit} (from $We=2.2$ to 1.5). The reverse is true for the sub-cell fe/fv -scheme, as here the We_{crit} -level actually increases (from $We=3.0$ to 3.3). Overall,

larger We_{crit} -levels are achieved with the fe/fv -scheme throughout all the various flow scenarios investigated. This is a persuasive argument to advocate the fe/fv -scheme over the alternate fe -scheme. This elevated level of We ($We=3.1$) for fe/fv , in compressible implementations, gives rise, once again, to post-corner oscillation, as noted above at earlier We -levels for incompressible flow.

Three-dimensional field plots

Surface plots presented in Figure 10 highlight the significant differences in solutions across the domain for the fe/fv -scheme at $We=3.0$. Viewing angles are displayed at the top of the figure. This covers incompressible ($Ma=0$, without relaxation, the extreme level) and compressible ($Ma=0.1$) flow configurations, along with variables of U-velocity (Figure 10a and c, viewing angle-1), stress τ_{xx} (Figure 10b and d, viewing angle-2), Mach number (Figure 10e, viewing angle-1) and density (Figure 10f, viewing angle-1). In contrast to the incompressible flow configuration, for the weakly-compressible flow, there is a sustained increase in U-velocity along the exit-channel, corresponding to the reduction in density there (see Figure 10f and 7b). In stress-peaks, both flows settings manifest the presence of the re-entrant corner singularity, yet with larger peaks in the compressible over the incompressible solutions. For the incompressible solution, beyond this position, along the exit-channel boundary wall, there is no growth in the stress-level. In the compressible solution, the stress sustains a monotonic growth along the wall, so that at the exit, the compressible- τ_{xx} doubles its incompressible counterpart (see Figure 9). This may be gathered from the more excessive cross-stream exit-flow curvature in the compressible τ_{xx} -surface plot.

Mach number contour patterns mimic those in velocity, confirming the acceleration of the flow throughout the exit-channel. Density patterns expose the influence of stress, in relating pressure to density. The three-dimensional surface plot at exit of Figure 10f is not straight, but curves towards the centerline, see also Figure 5b. Correspondingly, contours are straight at channel-entry, where density variation is negligible.

4.5. Flow patterns and vortex behaviour

In the contraction flow problem, salient-corner vortex-size and strength are major characteristics used to quantify numerical solutions, often judged against experimental observations. First, we summarise the position in the literature. In their experimental work, Evans and Walters [8] reported on both lip and salient-corner vortex behaviour. They attributed the complex characteristics encountered under vortex enhancement to several factors: material properties, type of geometric contraction (sharp or rounded), contraction ratio, fluid inertia and breakdown of steady flow. Prunode and Crochet [25] performed a

qualitative numerical comparison against these experimental results. Matallah *et al.*, [18] presented a comprehensive literature review on vortex activity, indicating the difficulty of accurate prediction of lip-vortex activity. The Matallah *et al.*, study was based on new features in the *fe*-scheme, with velocity-gradient recovery applied within the constitutive equation. There, for the creeping flow of an Oldroyd-B fluid, a lip-vortex appeared as early as $We=1.0$, which grew in intensity with increasing We . This lip-vortex strength was found to be larger than the salient-corner counterpart, from a We -level of unity and beyond. Likewise, based on *fv*-discretisation, Aboubacar and Webster [1], Xue *et al.*, [36], Oliveira and Pinho [22], also observed the appearance of a lip-vortex at $We=2.0$ in [1] and $We=1.6$ in [36]. Oliveira and Pinho [22] claimed to detect the appearance of a lip-vortex for an UCM model at $We=1.0$. Furthermore, the authors highlighted the need for a high degree of mesh refinement required for an accurate and reliable representation of vortex activity. The influence of inertia inclusion was also interrogated by Xue *et al.*, [36], who concluded that although fluid inertia had some influence on the upstream flow field, no evidence linked the appearance (or absence) of lip-vortices with inertia. On the contrary, Phillips and Williams [23] found that the inclusion of inertia for an Oldroyd-B model, delayed the appearance of the lip-vortex till $We=2.5$ (appearing at $We=2.0$ for $Re=0$) and the salient-corner vortex-size and intensity shrank (falling by about 20% below that for $Re=0$). Subsequently, Phillips and Williams [24] observed that the size of the salient-corner vortex decayed slowly over a range, $0 \leq We \leq 1.5$, where growth in vortex-intensity was independent of Re -level (0.0 or 1.0). Their results agreed closely with those of Sato and Richardson [26], Matallah *et al.*, [18] and Xue *et al.*, [36]. They also recognised the sensitivity of their results to the quality of mesh employed. Likewise, many authors have been aware of the impracticability to refine the mesh towards the corner beyond a certain threshold, due to the consequence of approximating the singularity. These findings demonstrate that trends in salient-corner vortex behaviour are better characterised and predicted than is the case for lip-vortex activity. In a more recent study, Alves *et al.*, [4] have catalogued a set of benchmark solutions, for Oldroyd-B and PTT models, again under planar creeping flow conditions. Solutions were produced based on a very fine mesh of $O(10^5)$ *fv*-cells (over one million degrees of freedom). Note here, our present mesh has $O(10^3)$ *fv*-cells. Oncemore, these authors demonstrated that vortex characteristics (size and intensity) were sensitive to the particular mesh employed. On their finest mesh, Alves *et al.*, also observed salient-corner vortex reduction with increasing We , and the appearance of a lip-vortex at around $We=1.0$ ($Re=0$). They found that, by extrapolating data on lip-vortex intensity through diminishing mesh-size[†], that for $We=0.5$ and

[†] Anticipating extrapolation to have some meaning, when applied to spatially shifting phenomena across meshes.

1.0, the lip-vortex would vanish. Yet, at $We=1.5$, a finite lip-vortex intensity ($0.02*10^3$) was predicted to survive, as mesh-size tended to zero.

As above, in our current study, the focus has been on flow patterns as a function of increasing We , emphasising steady-state salient vortex behaviour. Trends in vortex-size and intensity for both fe and fe/fv -schemes are presented under incompressible ($Ma=0$, without and with relaxation) and compressible ($Ma\approx 0$ and $Ma=0.1$) flow configurations. In addition, creeping ($Re=0.0$) and inertial ($Re=1.0$) conditions are considered. Extrema (minima) in stream-function intensity may be located either in the salient-corner vortex or lip-vortex depending on the particular We -level. Corner-vortex cell-size, X_s , is defined by convention as the non-dimensional vortex-length from the salient-corner to the separation-streamline along the upstream wall (see Figure 2a).

We begin with *scheme and flow setting comparison* for creeping flow. Under incompressible liquid flow, we illustrate in Figure 11 (as elsewhere to follow), vortex reduction trends in salient-corner vortex-size (top) and vortex-intensity (bottom, $*10^{-3}$), under both schemes and increasing We -level. Solutions are based on three alternative settings (incompressible flow, both with relaxation (R) and without (nR), and compressible flow with $Ma\approx 0$). Less than 1% difference is noted between the nR- and R-vortex-size data[‡]. For the compressible implementation, $Ma\approx 0$, and in contrast to its incompressible counterpart ($Ma=0$), discrepancies are uniformly around 2%.

Similarly, In Figure 12, we turn our attention to observing trends with switch in flow setting, detecting differences under scheme variants (fe and fe/fv), for flow settings nR-incompressible $Ma=0$ (left) and $Ma=0.1$ -compressible (right). Again vortex reduction is generally observed throughout all scenarios. Under incompressible considerations, there is barely any difference in solutions between the two numerical schemes (differences of about 2% in intensity and less than 0.1% in size). Close agreement is found between our solutions and those of Alves *et al.*, [4] (included in plot) up to relatively high levels of We of 2.5. For compressible flow conditions, fe and fe/fv -solutions differ by about 3% in size. Under any particular We -value, compressible conditions increase vortex characteristics compared to those for equivalent incompressible considerations (about 15% increase in size and intensity triples). As the characteristic compressible velocity scale (defined at the outlet) is larger than its incompressible counterpart (by about 30%, see Figure7b), this will have an effect on the We -scale employed. To equilibrate comparison, a transformed equivalent incompressible We -scale (We^*) is also included within the compressible plots. Even on this basis, compressibility exaggerates vortex characteristics.

[‡] This rises to one order more in vortex-intensity, due to the solution size $O(10^{-3})$ and the nature of this measure.

Streamline patterns with increasing We -level are plotted for each scheme, fe and hybrid fe/fv , and flow conditions, incompressible and weakly-compressible. For incompressible flow, relaxation is considered to reach elevated levels of We_{crit} . In Figure 13, under the fe/fv -scheme and creeping flow, streamlines contours are illustrated in steps of We (from 0.1 to We_{crit}) for incompressible (left) as well as compressible (right). We note, as stated above, the larger salient-corner-vortex, as well as the lip-vortex, in the compressible flow solutions above their incompressible counterparts. For incompressible flow solutions with the fe -scheme (not presented here), the lip-vortex first appears beyond $We=2.5$ ($1.9*10^{-4}$ at $We=2.8$). Alternatively, under the fe/fv -variant, the lip-vortex emerges earlier at $We=2.0$. This was the case in [3], there attributed to the characteristics of the hybrid scheme. In the compressible context, a lip-vortex first appears earlier (at $We=1.0$). Lip-vortex intensity becomes larger, in absolute value, for both flow configurations from the $We=3.0$ -level onwards[†]. Salient-corner vortex reduction is clearly apparent with increasing We under any flow configuration; whilst once present, lip-vortex size grows. For compressible flow, the shape of the salient vortex changes from its equivalent incompressible shape at $We=0.1$ (same in the Newtonian case) to a more stretched, and convex form joining the lip-vortex at high We .

Inertia inclusion: With restriction to fe -solutions henceforth, Figure 14 follows Figure 12, to demonstrate the influence of inclusion of inertia against increasing We -level. This data address $Ma\approx 0$ (left) as well as $Ma=0.1$ (right) compressible flow configurations. As anticipated, introducing inertia reduces vortex-size and intensity, a consistent trend noted across configurations. This reduction in size for incompressible flow ($Ma\approx 0$) varies between 17% for low values of We of 0.1, to 26% over the higher range at We of 1.5 (intensities following suit). Such trends in vortex-size are amplified for the compressible context ($Ma=0.1$) to 23% at low We of 0.1, up to 36% at $We=1.5$.

Following Figure 14, Figure 15 charts the equivalent compressible stream-function field solutions for inertial flow, under increasing We . The shrinkage of vortices (salient and lip) is clearly apparent compared to those in creeping flow. For the more ubiquitous lip-vortex activity, fe -solutions display no lip-vortex in the incompressible limit ($Ma\approx 0$), whilst one does appear at $We=1.0$ in the compressible ($Ma=0.1$) configuration, as was the case for compressible creeping flow. Again, at the relatively high limiting We of 2.0, lip-vortex intensity overtakes that of the salient-corner vortex. It has already been established [9,25], that in inertial flow there is delay in the onset of lip-vortex activity, compared to that under creeping flow. Its absence in the incompressible instance ($Ma\approx 0$) is due to the low We_{crit} (1.5) achieved by the $Ma\approx 0$ - fe -scheme (a lip-vortex appears at $We=2.0$ for creeping flow). Based

[†] For the compressible fe -scheme, not illustrated here, the lip-vortex also appears at $We=1.0$, with intensity of $3.7*10^{-4}$, increasing to $4.3*10^{-4}$ at $We_{crit}=1.7$.

on such observations, and specifically with respect to capture of corner solution characteristics, the sub-cell fe/fv -scheme is advocated over the parent- fe -variant.

5. Conclusions

We have investigated the abrupt four-to-one contraction benchmark problem for an Oldroyd-B model, two numerical schemes (fe and hybrid fe/fv), and three flow settings (incompressible- $Ma=0$, weakly-compressible- $Ma\approx 0$ and $Ma=0.1$). Solutions for both creeping and inertial flows conditions have been presented.

For each implementation, on We_{crit} and corresponding vortex activity (size and intensity), the main differences we observe against incompressible counterparts, lie in the sustained growth at constant rate, in both wall-stress components beyond the re-entrant corner. This is independent of the specific spatial scheme employed. Under the incompressible context, relaxation elevates the We_{crit} -levels for both scheme implementations, as numerical stability is enhanced. Larger We_{crit} levels are reached under all three flow settings, for the fe/fv -scheme compared to the fe -variant. This we attribute to the discretisation differences between schemes approaching the re-entrant corner: sub-cells and use of discontinuity capturing in the hybrid case. We note also, the property of the fe/fv -scheme to display some control on cross-stream solution variation, particularly in the presence of sharp solution gradients. On the vortex behaviour, at equitable We -level and flow settings, both schemes produce comparable vortex characteristics. We observed larger salient-corner and lip-vortices in compressible flow above its incompressible counterpart. Independently of flow setting, salient-corner vortex-size decays with increasing We (vortex reduction), whilst lip-vortex size is enhanced. For compressible flow, the shape of the salient vortex adopts a curved and stretched form (separation line becomes curved), uniting with the lip-vortex at high We . Upon introducing inertia into the problem, all aspects of vortex (salient and lip) activities are reduced accordingly.

Further extensions to the current study shall be oriented towards seeking true transient solutions and introducing alternative rheological models.

Appendix: Efficiency in computation of LMN flows

In LMN flows, the largest eigenvalue of the system (λ_{\max}) tends toward the speed of sound, whilst the smallest (λ_{\min}) provides the speed of the fluid. The condition number of the system ($k = \lambda_{\max} / \lambda_{\min}$), goes large as the Mach number approaches zero, upholding

$$k = \frac{u + c}{u} = 1 + Ma^{-1}. \quad (21)$$

This situation correspondingly increases the stiffness in the system [29]. Consequently, for compressible implicit schemes, iterative solution of the algebraic equation system is slow and expensive. On the other hand, time-marching explicit schemes suffer from excessively small time-steps to satisfy CFL conditions. This imposes restriction on time-step selection of the form,

$$\Delta t_{comp} \leq a \frac{\Delta x}{u + c}, \quad (22)$$

where, a is a constant of order unity, Δx the mesh length-scale, and $(u+c)$ is the speed of the acoustic mode. For the incompressible counterpart, the stability restriction is less severe:

$$\Delta t_{inc} \leq a \frac{\Delta x}{u}, \quad (23)$$

where, the time-step is in balance with the physical time-scale. One can obtain

$$\frac{\Delta t_{comp}}{\Delta t_{inc}} = \frac{Ma}{Ma + 1} \rightarrow 0 \quad \text{as } Ma \rightarrow 0. \quad (24)$$

Thus, for LMN and explicit schemes, acoustic waves impose a much smaller time-step than the physical time-step. Therefore, conventional compressible solvers for LMN flows, either in explicit or implicit form, become inefficient and impractical without modification for $Ma < 0.3$. The problem can be quantified on the following grounds: the speed of sound for air at room temperature is around 330 m/s. Therefore at $Ma = 0.3$, the speed of the fluid will be approximately 100 m/s. Nevertheless, the speed of sound for compressible liquids is much faster than the speed of sound in air (say five times). In applications such as polymer processing, velocity levels are generally low (of the order of unity). Therefore, system condition numbers in compressible liquid flows are normally smaller, by an order of magnitude, comparable to those for compressible gas dynamic applications. This is why computation of compressible liquid flows is generally associated with much more severe conditions than those for gas flows.

Acknowledgements: The financial support of EPSRC grant GR/R46885/01 is gratefully acknowledged.

References

- [1] M. Aboubacar, M.F. Webster, A cell-vertex finite volume/element method on triangles for abrupt contraction viscoelastic flows, *Journal of Non-Newtonian Fluid Mechanics* **98** (2001) 83-106.
- [2] M. Aboubacar, H. Matallah, M.F. Webster, Highly elastic solutions for Oldroyd-B and Phan-Thien/Tanner fluids with a finite volume/element method: planar contraction flows, *Journal of Non-Newtonian Fluid Mechanics* **103** (2002) 65-103.
- [3] M. Aboubacar, H. Matallah, H.R. Tamaddon-Jahromi, M.F. Webster, Numerical prediction of extensional flows in contraction geometries: hybrid finite volume/element method, *Journal of Non-Newtonian Fluid Mechanics* **104** (2002) 125-164.
- [4] M.A. Alves, P.J. Oliveira, F.T. Pinho, Benchmark solutions for the flow of Oldroyd-B and PTT fluids in planar contractions, *Journal of Non-Newtonian Fluid Mechanics* **110** (2003) 45-75.
- [5] P.T.F. Baaijens, Mixed finite element methods for viscoelastic flow analysis: a review, *Journal of Non-Newtonian Fluid Mechanics* **79** (1998) 361-385.
- [6] E.A. Brujan, A first-order model for bubble dynamics in a compressible viscoelastic liquid, *Journal of Non-Newtonian Fluid Mechanics* **84** (1999) 83-103.
- [7] E.O.A. Carew, P. Townsend, M.F. Webster, A Taylor-Petrov-Galerkin algorithm for viscoelastic flow, *Journal of Non-Newtonian Fluid Mechanics* **50** (1993) 253-287.
- [8] R.E. Evans, K. Walters, Flow characteristics associated with abrupt changes in geometry in the case of highly elastic liquids, *Journal of Non-Newtonian Fluid Mechanics* **20** (1986) 11-29.
- [9] R.E. Evans, K. Walters, Further remarks on the lip-vortex mechanism of vortex enhancement in planar-contraction flows, *Journal of Non-Newtonian Fluid Mechanics* **32** (1989) 95-105.
- [10] G.C. Georgiou, The time-dependent, compressible Poiseuille and extrudate-swell flows of a Carreau fluid with slip at the wall, *Journal of Non-Newtonian Fluid Mechanics* **109** (2003) 93-114.
- [11] R. Guénette, M. Fortin, A new mixed finite element method for computing viscoelastic flows, *Journal of Non-Newtonian Fluid Mechanics* **60** (1995) 27-52.
- [12] F.H. Harlow, A. Amsden, Numerical calculation of almost incompressible flow, *Journal of Computational Physics* **3** (1968) 80-93.
- [13] K. Karki, S.V. Patankar, pressure based calculation procedure for viscous flows at all speeds in arbitrary configurations, *AIAA journal* **27** (1989) 1167-1174.
- [14] I.J. Keshtiban, F. Belblidia, M.F. Webster, Numerical simulation of compressible viscoelastic liquids. In: *Journal of Non-Newtonian Fluid Mechanics*, special issue,

- XIIIth** International Workshop on Numerical Methods for non-Newtonian Flows, Lausanne, Switzerland, 2003.
- [15] R. Keunings, On the high Weissenberg number problem, *Journal of Non-Newtonian Fluid Mechanics* **20** (1986) 209-226.
- [16] R.C. King, M.R. Apelian, R.C. Armstrong, R.A. Brown, Numerically stable finite element techniques for viscoelastic calculations in smooth and singular geometries, *Journal of Non-Newtonian Fluid Mechanics* **29** (1988) 147-216.
- [17] K. Lee, M.R. Mackley, The application of the multi-pass rheometer for precise rheo-optic characterisation of polyethylene melts, *Chemical Engineering Science* **56** (2001) 5653-5661.
- [18] H. Matallah, P. Townsend, M.F. Webster, Recovery and stress-splitting schemes for viscoelastic flows, *Journal of Non-Newtonian Fluid Mechanics* **75** (1998) 139-166.
- [19] S. Mittal, T. Tezduyar, A unified finite element formulation for compressible and incompressible flows using augmented conservation variables, *Computer Methods in Applied Mechanics and Engineering* **161** (1998) 229-243.
- [20] G. Mompean, On predicting abrupt contraction flows with differential and algebraic viscoelastic models, *Computers & Fluids* **31** (2002) 935-956.
- [21] C.D. Munz, S. Roller, R. Klein, K.J. Geratz, The extension of incompressible flow solvers to the weakly compressible regime, *Computers & Fluids* **32** (2003) 173-196.
- [22] P.J. Oliveira, F.T. Pinho, Plane contraction flows of upper convected Maxwell and Phan-Thien-Tanner fluids as predicted by a finite-volume method, *Journal of Non-Newtonian Fluid Mechanics* **88** (1999) 63-88.
- [23] T.N. Phillips, A.J. Williams, Viscoelastic flow through a planar contraction using a semi-Lagrangian finite volume method, *Journal of Non-Newtonian Fluid Mechanics* **87** (1999) 215-246.
- [24] T.N. Phillips, A.J. Williams, Comparison of creeping and inertial flow of an Oldroyd B fluid through planar and axisymmetric contractions, *Journal of Non-Newtonian Fluid Mechanics* **108** (2002) 25-47.
- [25] B. Purnode, M.J. Crochet, Flows of polymer solutions through contractions Part 1: flows of polyacrylamide solutions through planar contractions, *Journal of Non-Newtonian Fluid Mechanics* **65** (1996) 269-289.
- [26] T. Sato, S.M. Richardson, Explicit numerical simulation of time-dependent viscoelastic flow problems by a finite element/finite volume method, *Journal of Non-Newtonian Fluid Mechanics* **51** (1994) 249-275.
- [27] P.G. Tait, *HSMO, London* **2** (1888).
- [28] P. Townsend, M.F. Webster, An algorithm for the three-dimensional transient simulation of non-Newtonian fluid flows. In: M.J. G.N. Pande G.N., Nijhoff, Kluwer,

- Dordrecht (Ed.), *Transient/Dynamic Analysis and Constitutive Laws for Engineering Materials*, Int. Conf. Numerical Methods in Engineering: Theory and Applications - NUMETA 87", eds., Vol. 2, T12, 1987, pp. 1-11.
- [29] E. Turkel, Preconditioned Methods for solving the incompressible and low speed compressible equations, *journal of computational physics* **72** (1987) 277-298.
- [30] J. Van Kan, A second-order accurate pressure-correction scheme for viscous incompressible flow, *SIAM J. Sci. Stat. Comput.* **7** (1986) 870-891.
- [31] J. Van Kan, A second-order accurate pressure-correction scheme for viscous incompressible flow, *SIAM Journal of Scientific and Statistical Computing* **7** (1986) 870-891.
- [32] P. Wapperom, M.F. Webster, Simulation for viscoelastic flow by a finite volume/element method, *Computer Methods in Applied Mechanics and Engineering* **180** (1999) 281-304.
- [33] N.D. Waters, M.J. King, Unsteady flow of an elastico-viscous liquid, *Rheology Acta* **19** (1970) 171-190.
- [34] M.F. Webster, I.J. Keshtiban, F. Belblidia, Computation of weakly-compressible highly-viscous polymeric liquid flows, *Report No.: CSR 11-2003*: Computer Science Dept., University of Wales Swansea, UK.
- [35] J.S. Wong, D.L. Darmofal, J. Peraire, The solution of the compressible Euler equations at low Mach numbers using a stabilized finite element algorithm, *Computer Methods in Applied Mechanics and Engineering* **190** (2001) 5719-5737.
- [36] S.C. Xue, N. Phan-Thien, R.I. Tanner, Three dimensional numerical simulations of viscoelastic flows through planar contractions, *Journal of Non-Newtonian Fluid Mechanics* **74** (1998) 195-245.
- [37] F. Yurun, A comparative study of the discontinuous Galerkin and continuous SUPG finite element methods for computation of viscoelastic flows, *Computer Methods in Applied Mechanics and Engineering* **141** (1997) 47-65.

List of Figures

- Table 1. Critical We level for different scheme variants and flow configurations.
- Figure 1. Hybrid fe/fv spatial discretization, a) schematic diagram of fe -cell with 4 fv sub-cells, b) LDB-scheme, defining angles in fv -cell, c) MDC area for node l .
- Figure 2. a) Contraction flow schema, b) Mesh around the contraction
- Figure 3. Incompressible field contours, $We=1.5$, $Re=0.0$: a) P , b) τ_{xx} , c) τ_{xy} , d) Ψ ; (left) fe , (right) fe/fv implementations.
- Figure 4. Incompressible (without relaxation, nR; with relaxation, R) stress profiles at horizontal line $y=3.0$, $We=1.5$, $Re=0.0$: (top) τ_{xx} , (bottom) τ_{xy} ; (left) fe , (right) fe/fv implementations.
- Figure 5. Compressible ($Ma=0.1$) field contours, $We=1.5$, $Re=0.0$: a) P , b) ρ , c) τ_{xx} , d) τ_{xy} , e) Ψ ; (left) fe , (right) fe/fv implementations.
- Figure 6. Compressible ($Ma=0.1$) stress profiles at horizontal line $y=3.0$, $We=1.5$, $Re=0.0$: (top) τ_{xx} , (bottom) τ_{xy} ; (left) fe , (right) fe/fv implementations.
- Figure 7. U-velocity profiles at centreline, $We=1.5$, $Re=0.0$: (top) fe vs. fe/fv : a) incompressible, b) compressible; (bottom) incompressible vs. $Ma \approx 0$ limit: c) fe , d) fe/fv implementations.
- Figure 8. N_1 -profiles at horizontal line $y=3.0$ increasing We , $Re=0.0$. Incompressible: (left) fe and (right) fe/fv implementations; (top) without relaxation, (bottom) with relaxation.
- Figure 9. N_1 -profiles at horizontal line $y=3.0$, increasing We , $Re=0.0$. Compressible: (left) fe and (right) fe/fv implementations; (top) incompressible limit, $Ma=0$; (bottom) compressible $Ma=0.1$.
- Figure 10. 3D contour plots, fe/fv scheme, $We=3.0$, $Re=0.0$. Incompressible a) U-velocity, b) stress τ_{xx} ; Compressible c) U-velocity, d) stress τ_{xx} , e) Ma and f) ρ .
- Figure 11. Vortex size (top) and intensity (bottom, $\cdot 10^{-3}$), increasing We : incompressible creeping flow; fe (left) and fe/fv (right) schemes; relaxed, non-relaxed and $Ma \approx 0$ variants.
- Figure 12. Vortex size (top) and intensity (bottom, $\cdot 10^{-3}$), increasing We : incompressible (nR) ($Ma=0$, left) and compressible ($Ma=0.1$, right); creeping flow, comparison of fe and fe/fv solutions.
- Figure 13. Streamline contours, increasing We : (left) incompressible (R) and (right) compressible; creeping flows, fe/fv scheme, vortex intensity $\cdot 10^{-3}$.
- Figure 14. Vortex size (top) and intensity (bottom, $\cdot 10^{-3}$), increasing We , compressible fe -scheme: $Ma \approx 0$ (left) and $Ma=0.1$ (right); creeping vs. inertial flow.
- Figure 15. Streamline contours, increasing We : (left) incompressible and (right) compressible; inertial flows, fe scheme, vortex intensity $\cdot 10^{-3}$.

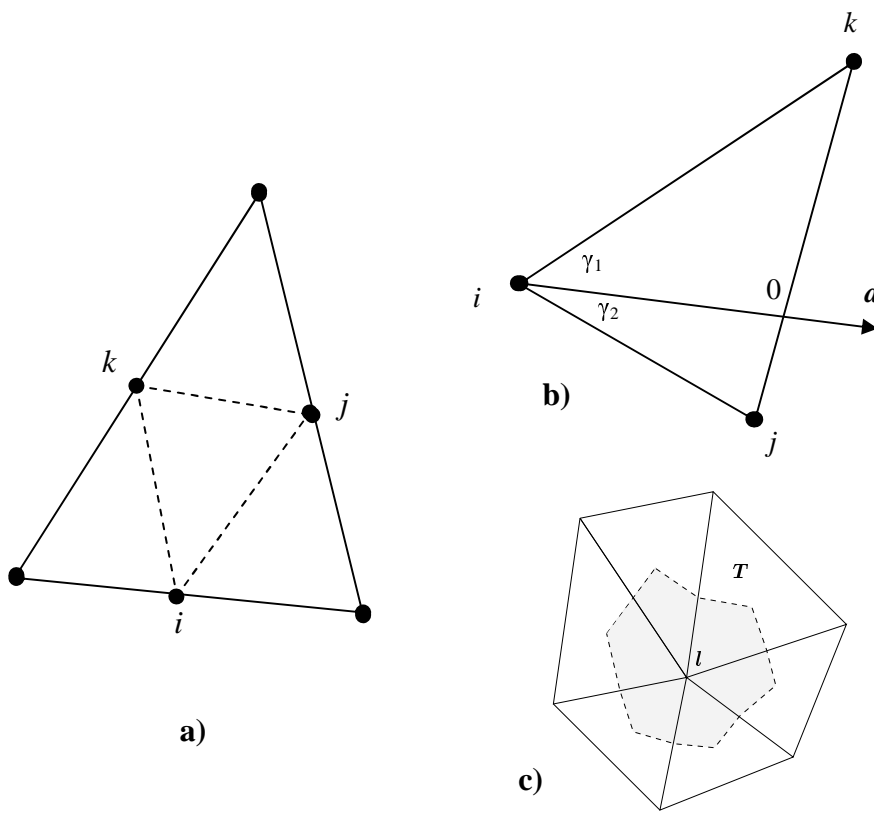
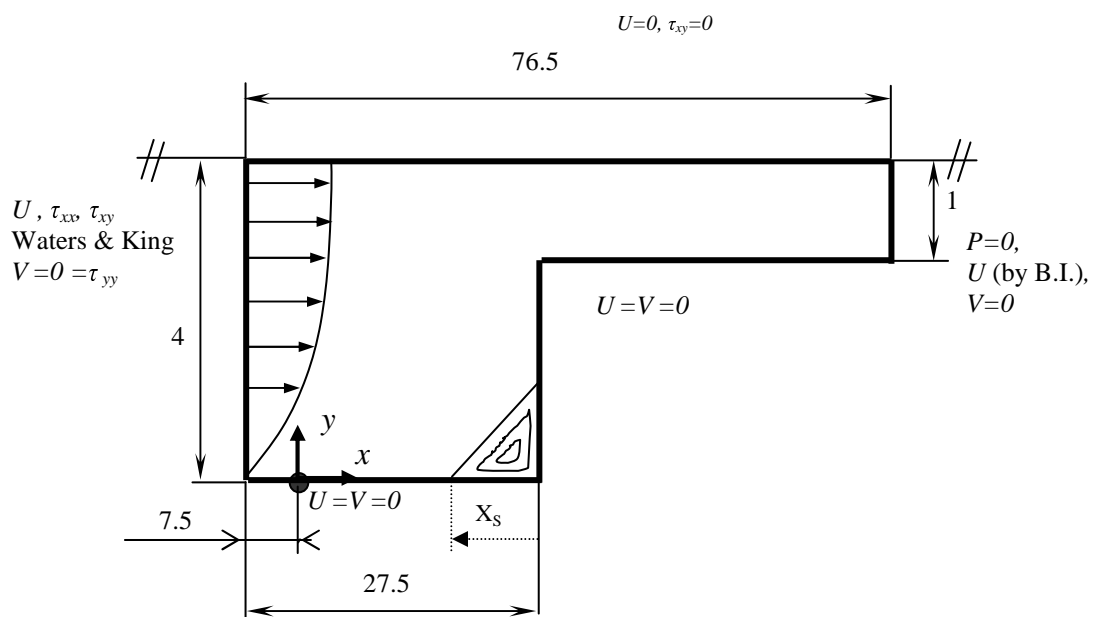
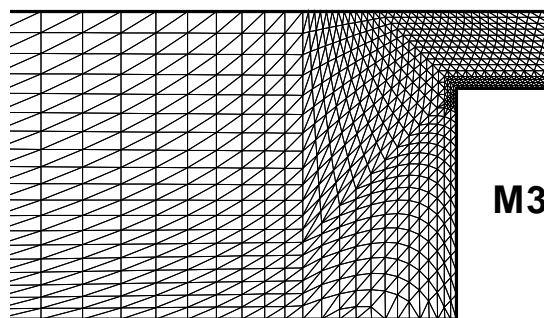


Figure 1. Hybrid fe/fv spatial discretization, a) schematic diagram of fe-cell with 4 fv sub-cells, b) LDB-scheme, defining angles in fv cell, c) MDC area for node l .



a)



b)

Figure 2. a) Contraction flow schema, b) Mesh around the contraction

Incompressible, $We=1.5, Re=0.0$

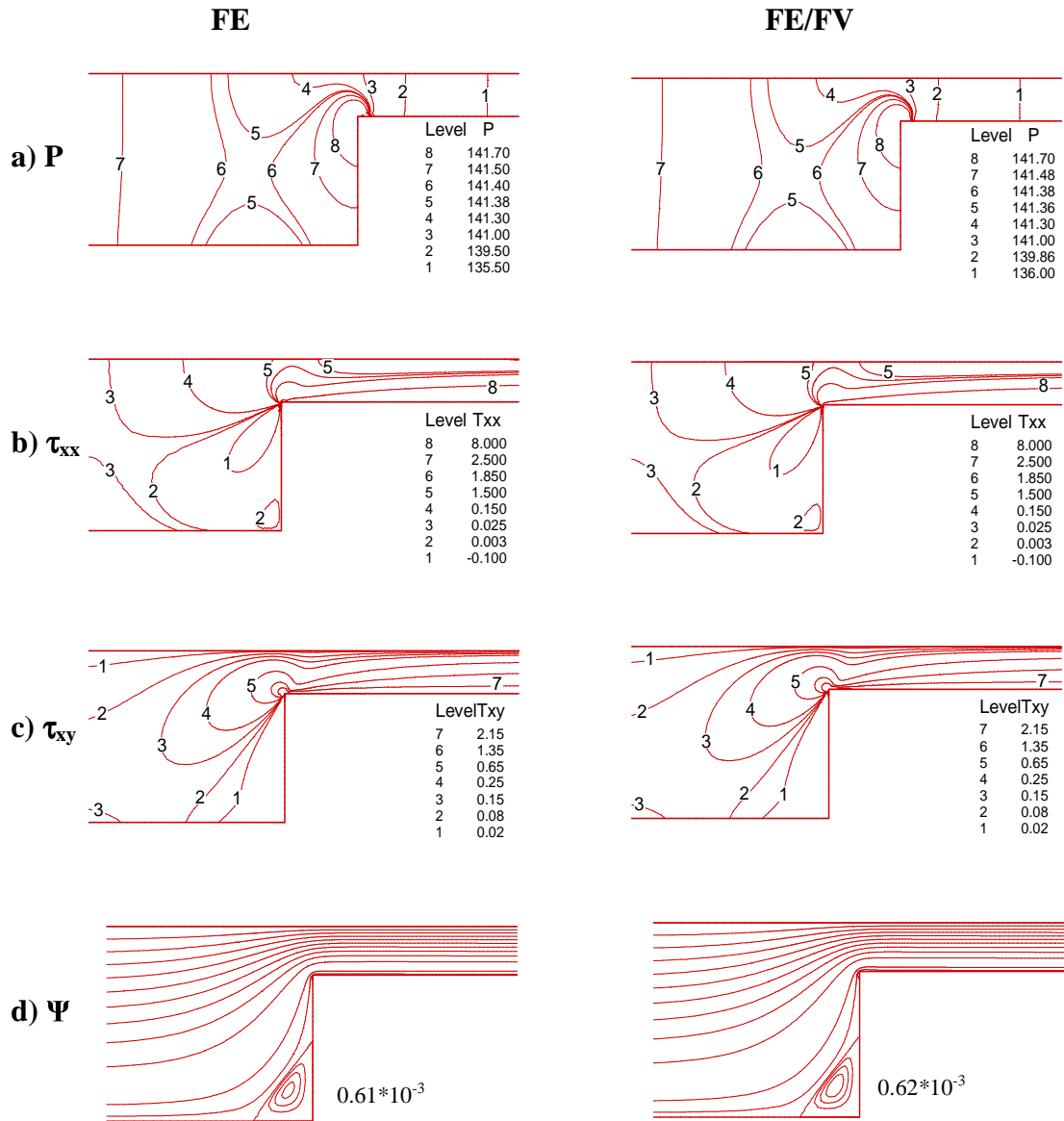


Figure 3. Incompressible field contours, $We=1.5, Re=0.0$: a) P, b) τ_{xx} , c) τ_{xy} , d) Ψ ; (left) *fe*, (right) *fe/fv* implementations.

Incompressible, $We=1.5$, $Re=0.0$

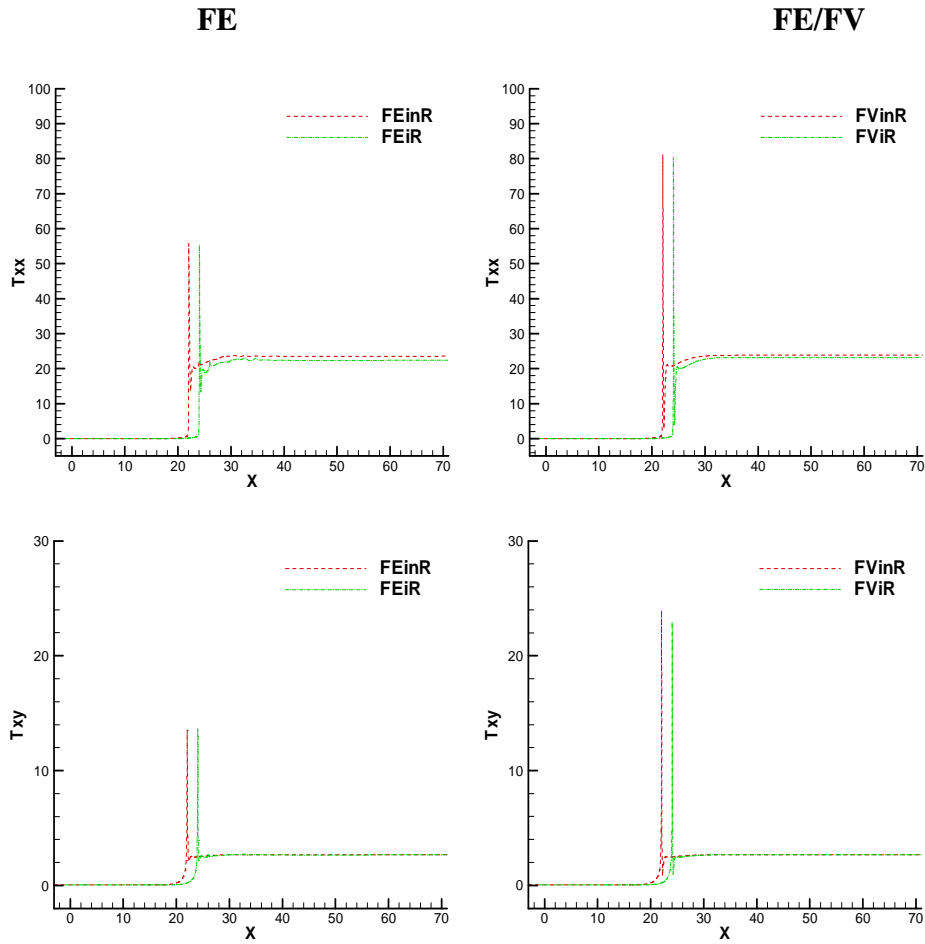


Figure 4. Incompressible (without relaxation, nR; with relaxation, R) stress profiles at horizontal line $y=3.0$, $We=1.5$, $Re=0.0$: (top) τ_{xx} , (bottom) τ_{xy} ; (left) fe , (right) fe/fv implementations.

Compressible, $We=1.5, Re=0.0$

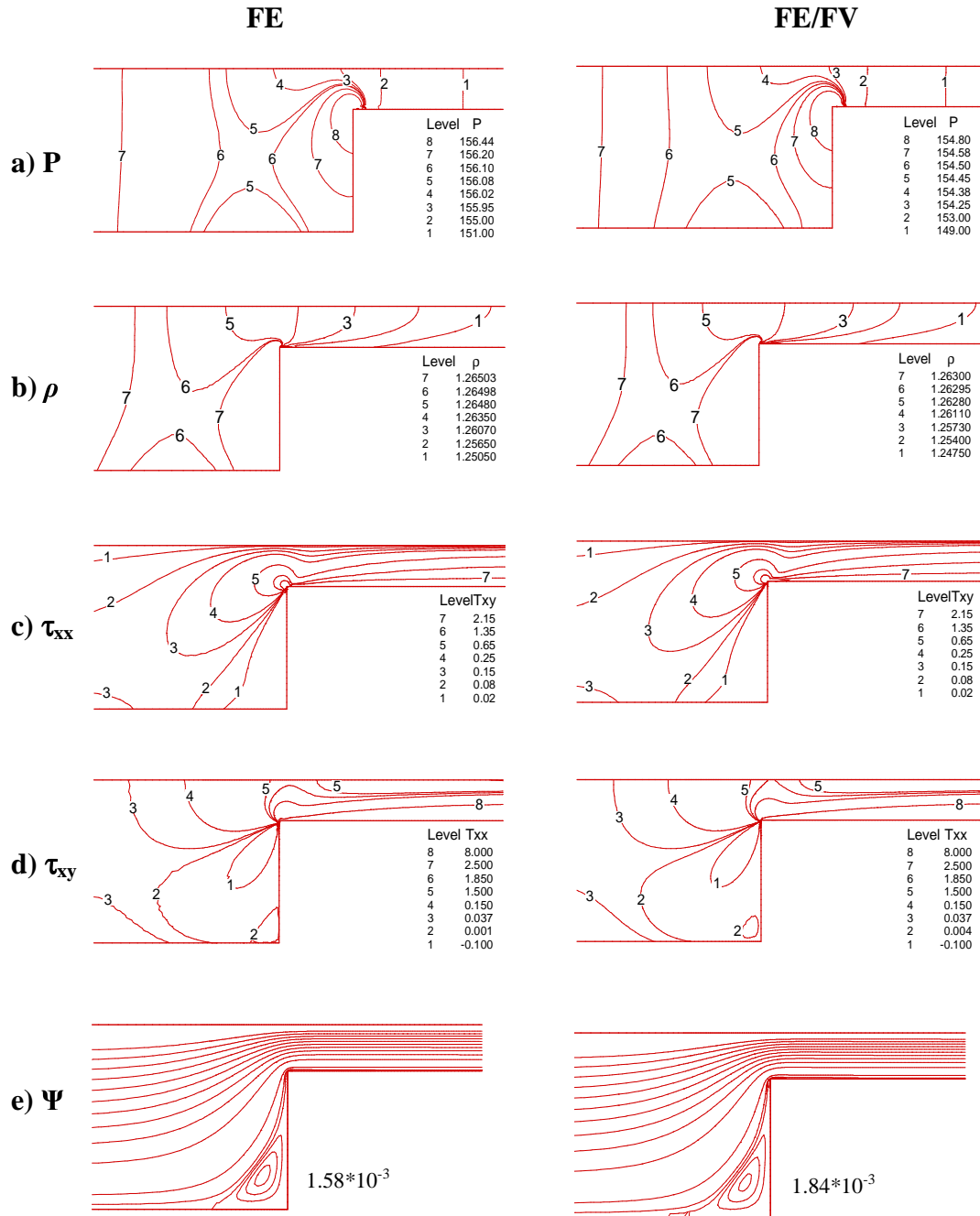


Figure 5. Compressible ($Ma=0.1$) field contours, $We=1.5, Re=0.0$: a) P, b) ρ , c) τ_{xx} , d) τ_{xy} , e) Ψ ; (left) *fe*, (right) *fe/fv* implementations.

Compressible, $We=1.5$, $Re=0.0$

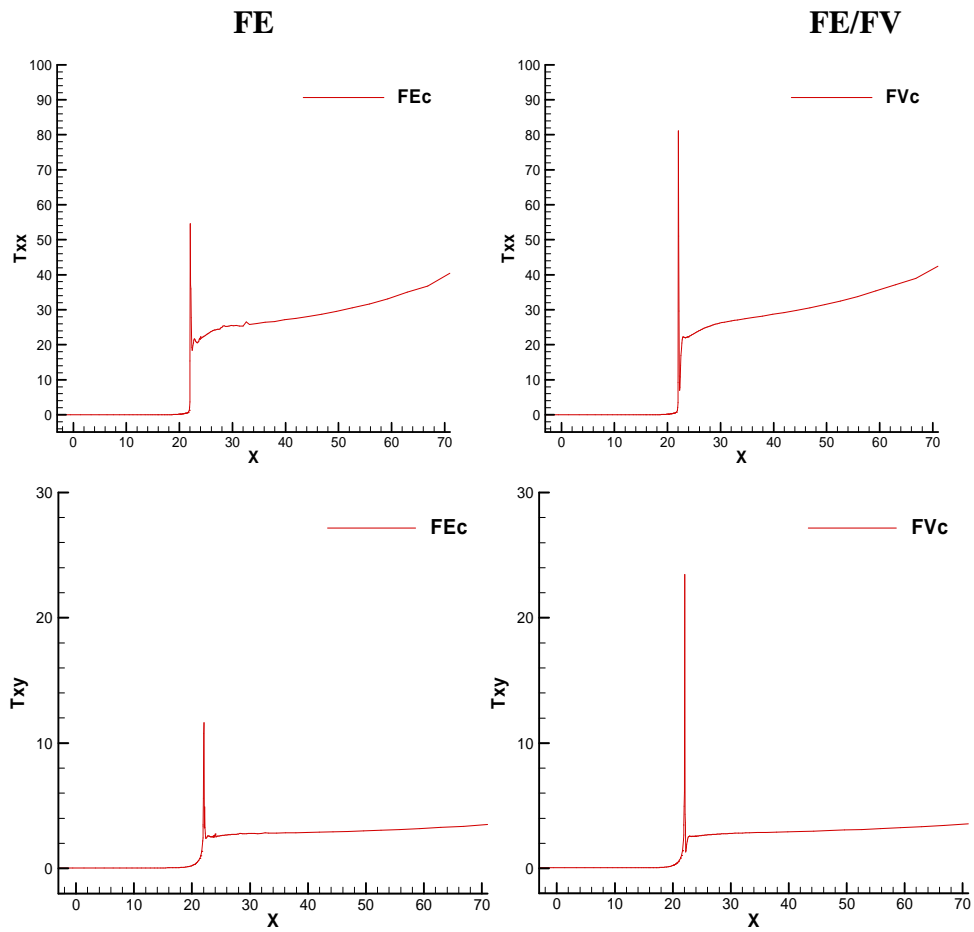


Figure 6. Compressible ($Ma=0.1$) stress profiles at horizontal line $y=3.0$, $We=1.5$, $Re=0.0$: (top) τ_{xx} , (bottom) τ_{xy} ; (left) fe , (right) fe/fv implementations.

$We=1.5, Re=0.0$

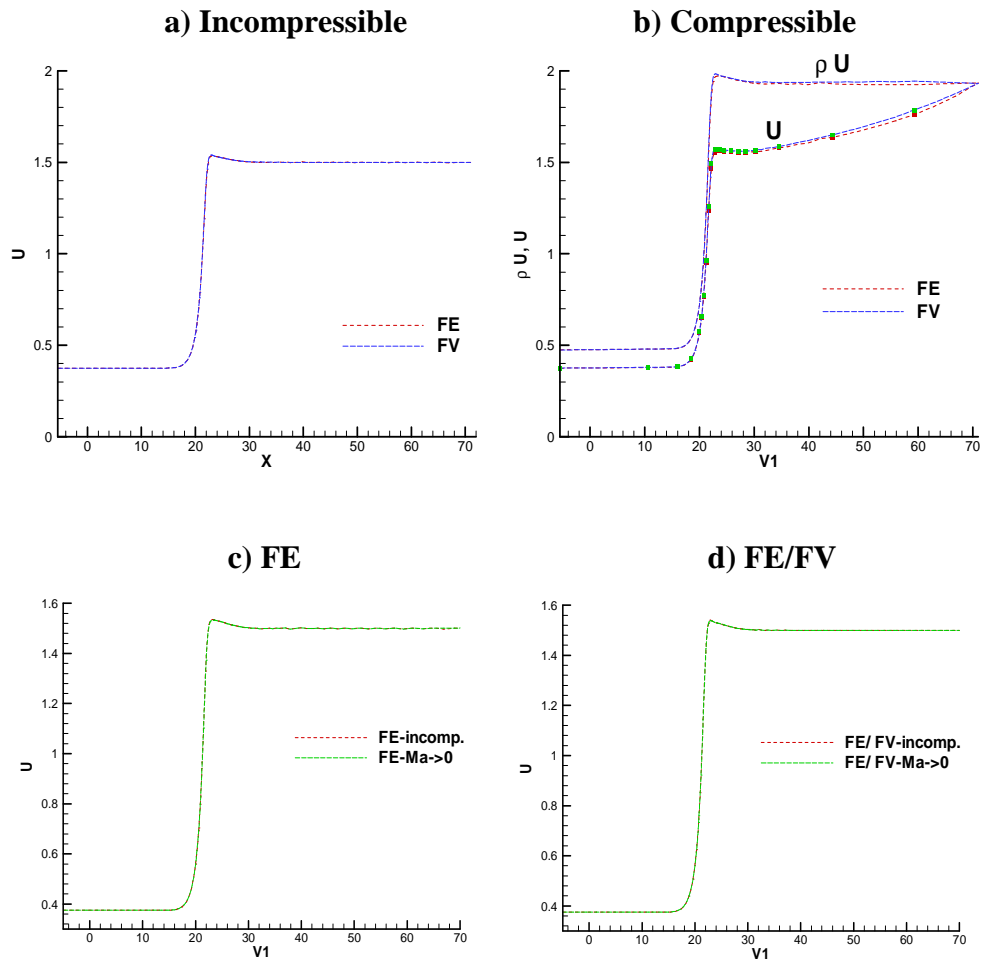


Figure 7. U-velocity profiles at centreline, $We=1.5, Re=0.0$: (top) fe vs. fe/fv : a) incompressible, b) compressible; (bottom) incompressible vs. $Ma \approx 0$ limit: c) fe , d) fe/fv implementations.

Incompressible, $We \uparrow$, $Re=0.0$

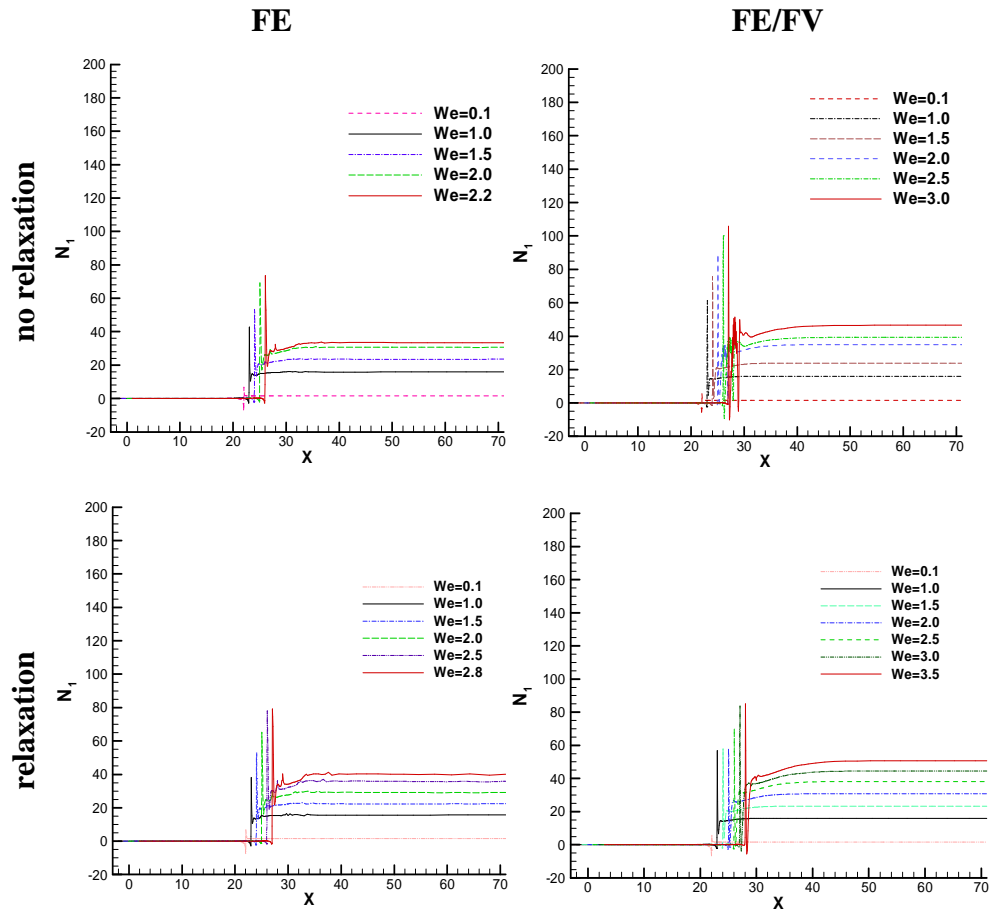


Figure 8. N_1 -profiles at horizontal line $y=3.0$ increasing We , $Re=0.0$. Incompressible: (left) fe and (right) fe/fv implementations; (top) without relaxation, (bottom) with relaxation.

Compressible, $We \uparrow$, $Re=0.0$

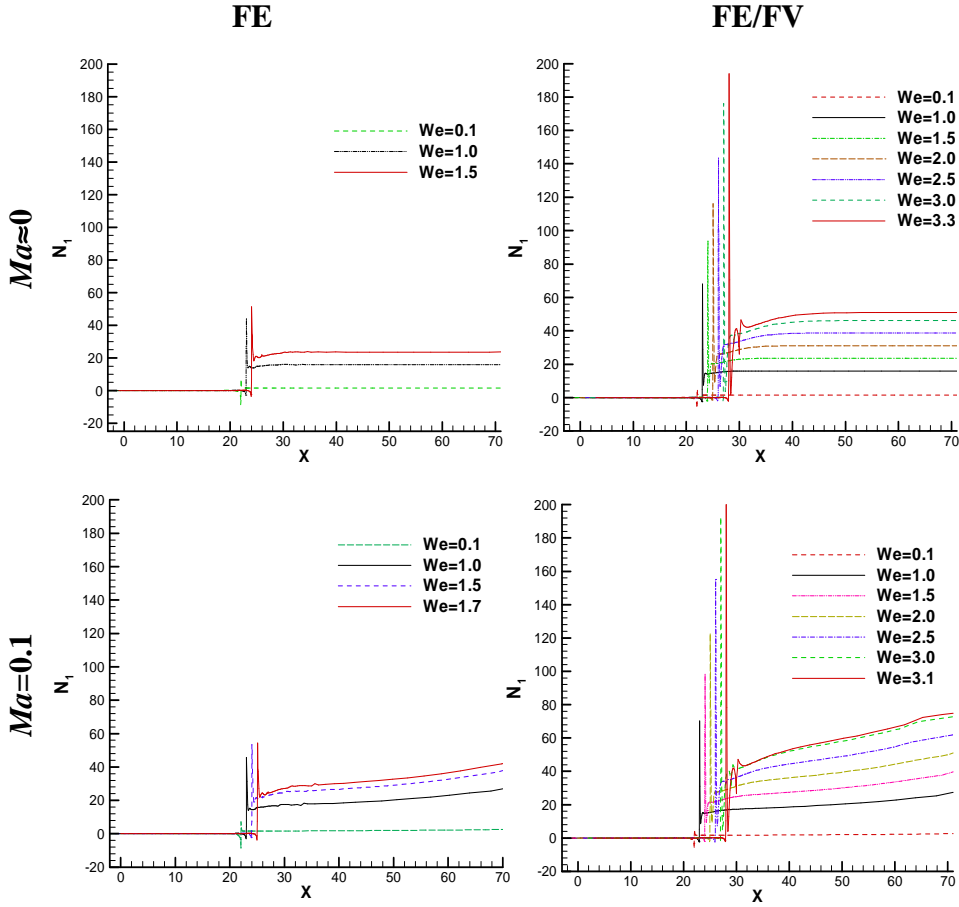


Figure 9. N_1 -profiles at horizontal line $y=3.0$, increasing We , $Re=0.0$. Compressible: (left) fe and (right) fe/fv implementations; (top) incompressible limit, $Ma=0$; (bottom) compressible $Ma=0.1$.

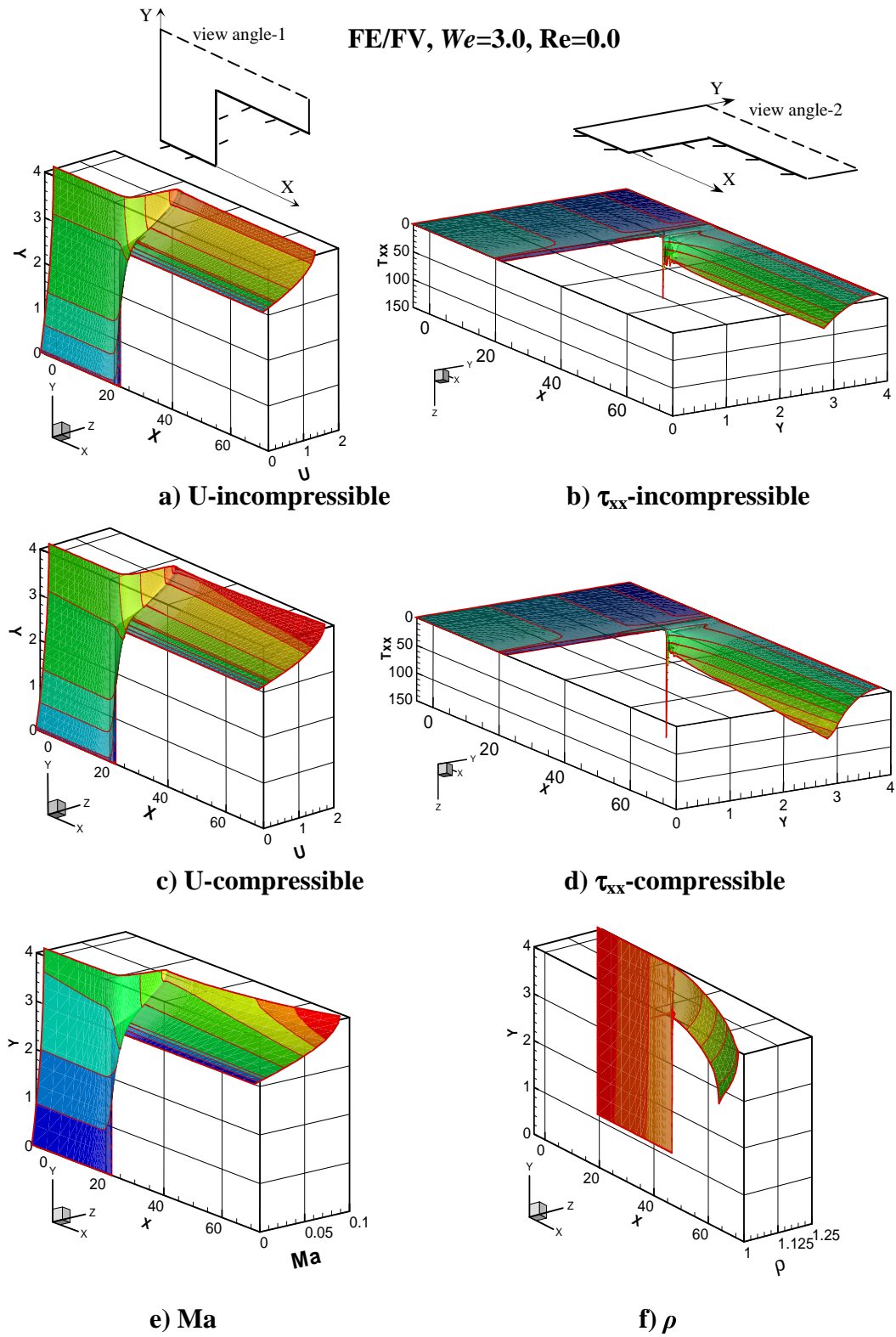


Figure 10. 3D contour plots, fe/fv scheme, $We=3.0$, $Re=0.0$. Incompressible a) U-velocity, b) stress τ_{xx} ; Compressible c) U-velocity, d) stress τ_{xx} , e) Ma and f) ρ .

Incompressible, $We \uparrow$, $Re=0.0$

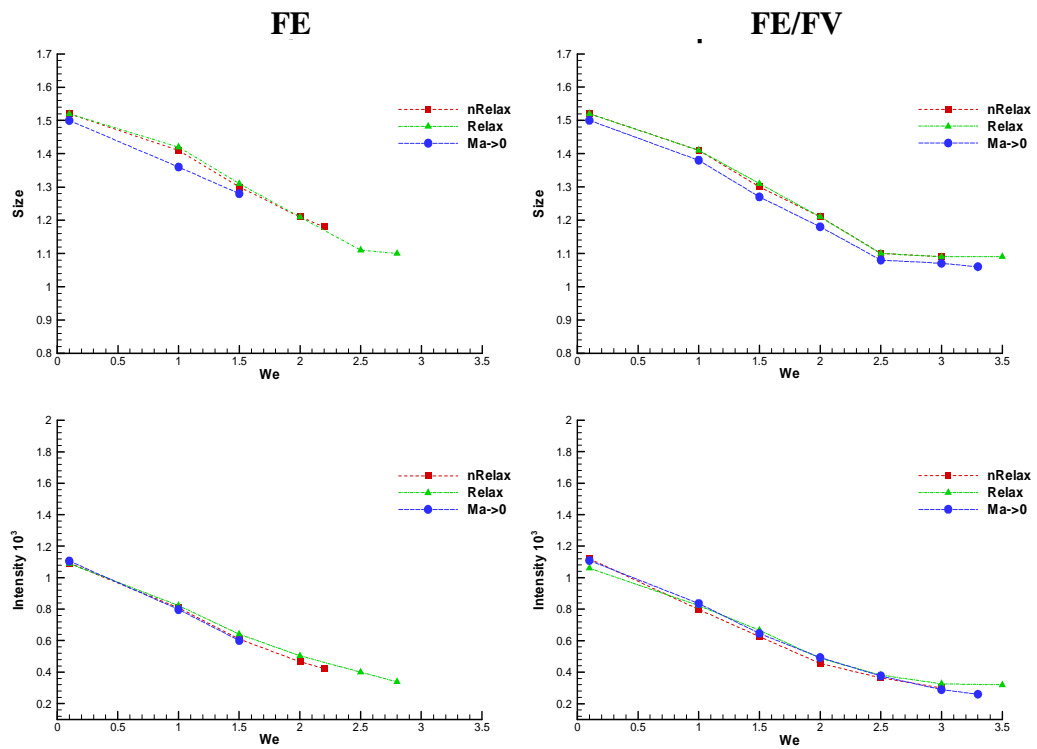


Figure 11. Vortex size (top) and intensity (bottom, $\cdot 10^{-3}$), increasing We : incompressible creeping flow; fe (left) and fe/fv (right) schemes; relaxed, non-relaxed and $Ma \approx 0$ variants.

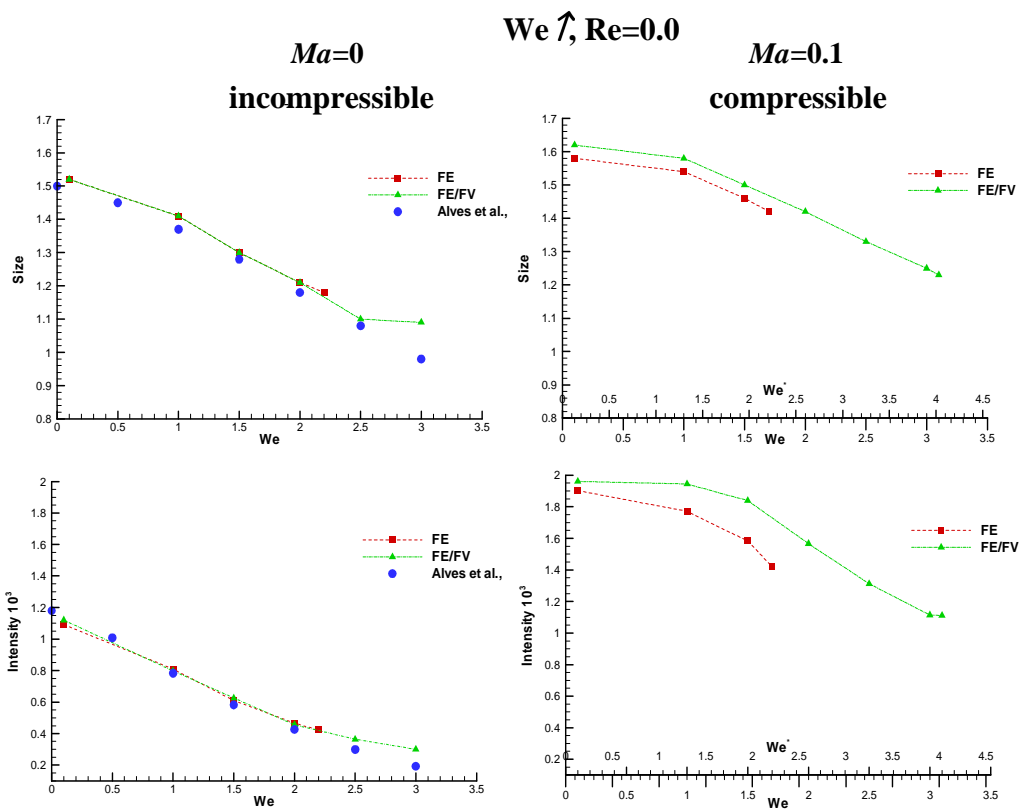


Figure 12. Vortex size (top) and intensity (bottom, $\cdot 10^{-3}$), increasing We : incompressible (nR) ($Ma=0$, left) and compressible ($Ma=0.1$, right); creeping flow, comparison of fe and fe/fv solutions.

FE/FV scheme, $We \uparrow$, $Re=0.0$

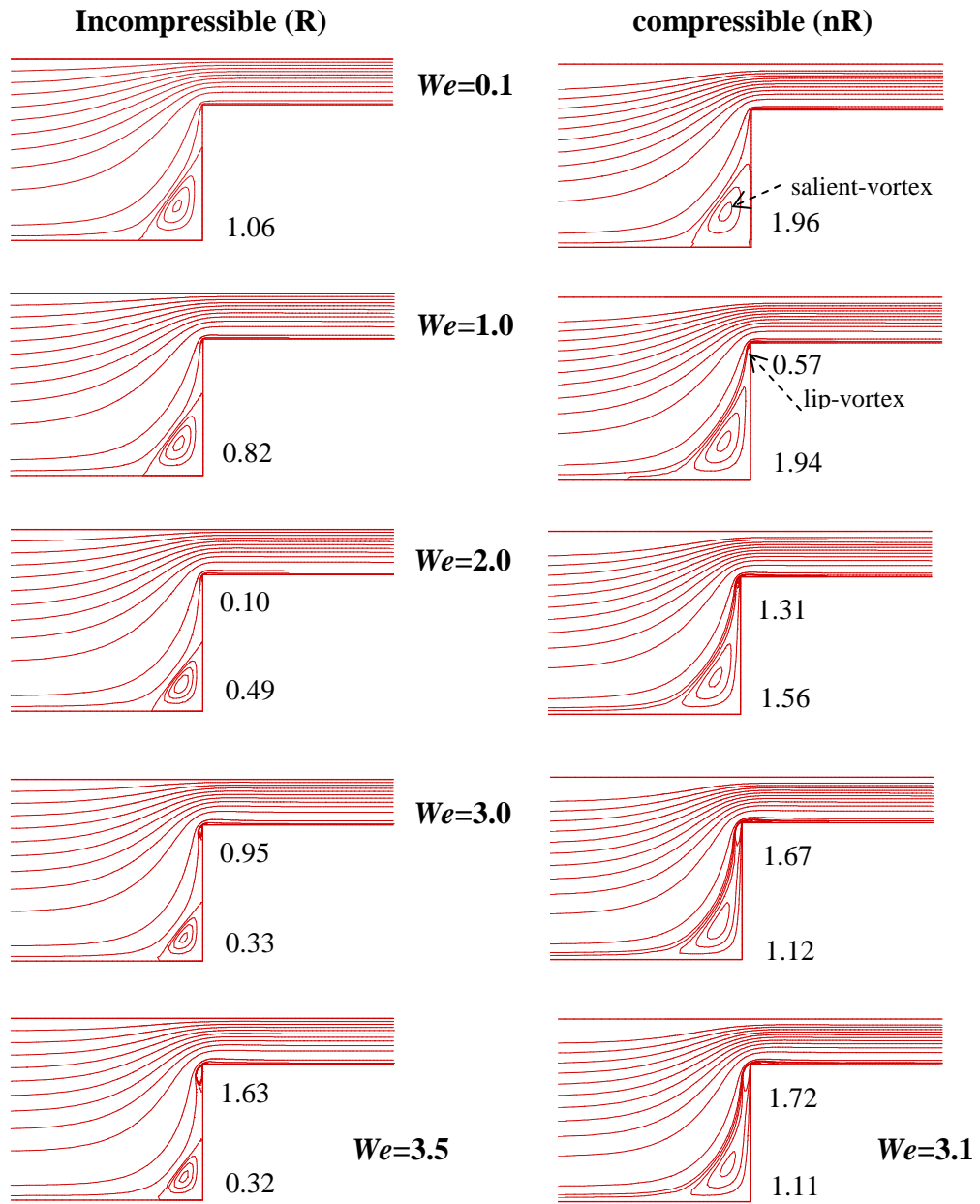


Figure 13. Streamline contours, increasing We : (left) incompressible (R) and (right) compressible (nR); creeping flows, fe/fv scheme, vortex intensity* 10^{-3} .

Compressible, FE scheme, $We \uparrow$, $Re=0.0$, $Re=1.0$

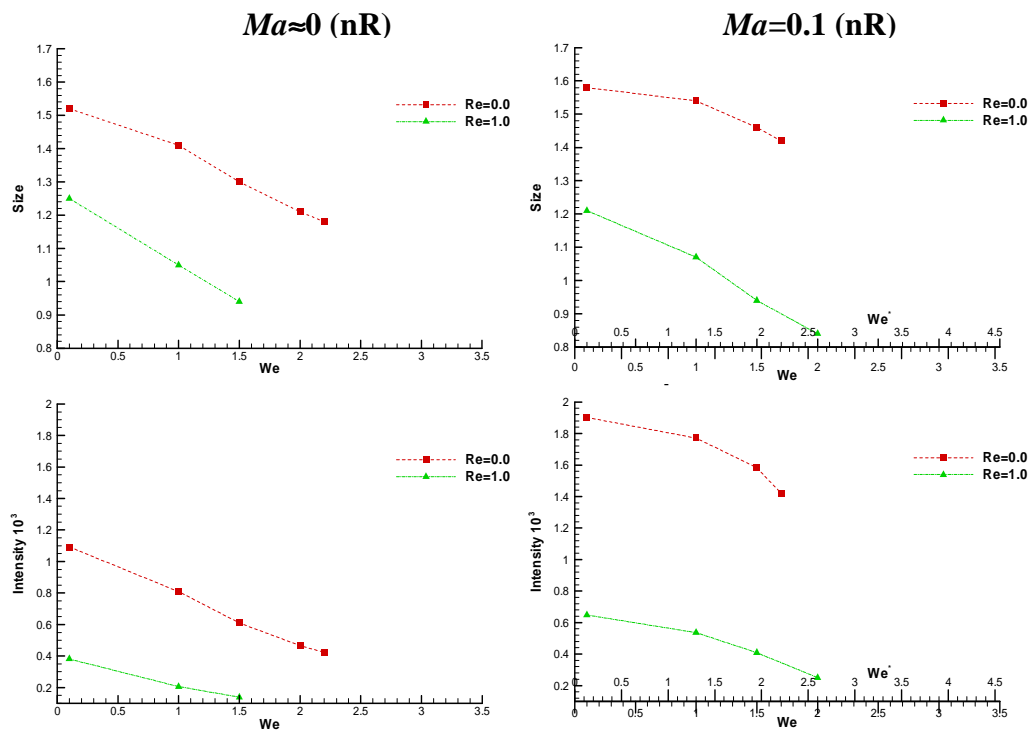


Figure 14. Vortex size (top) and intensity (bottom, $\cdot 10^{-3}$), increasing We , compressible fe -scheme: $Ma \approx 0$ (left) and $Ma = 0.1$ (right); creeping vs. inertial flow.

Compressible, FE scheme, $We \uparrow$, $Re=1.0$

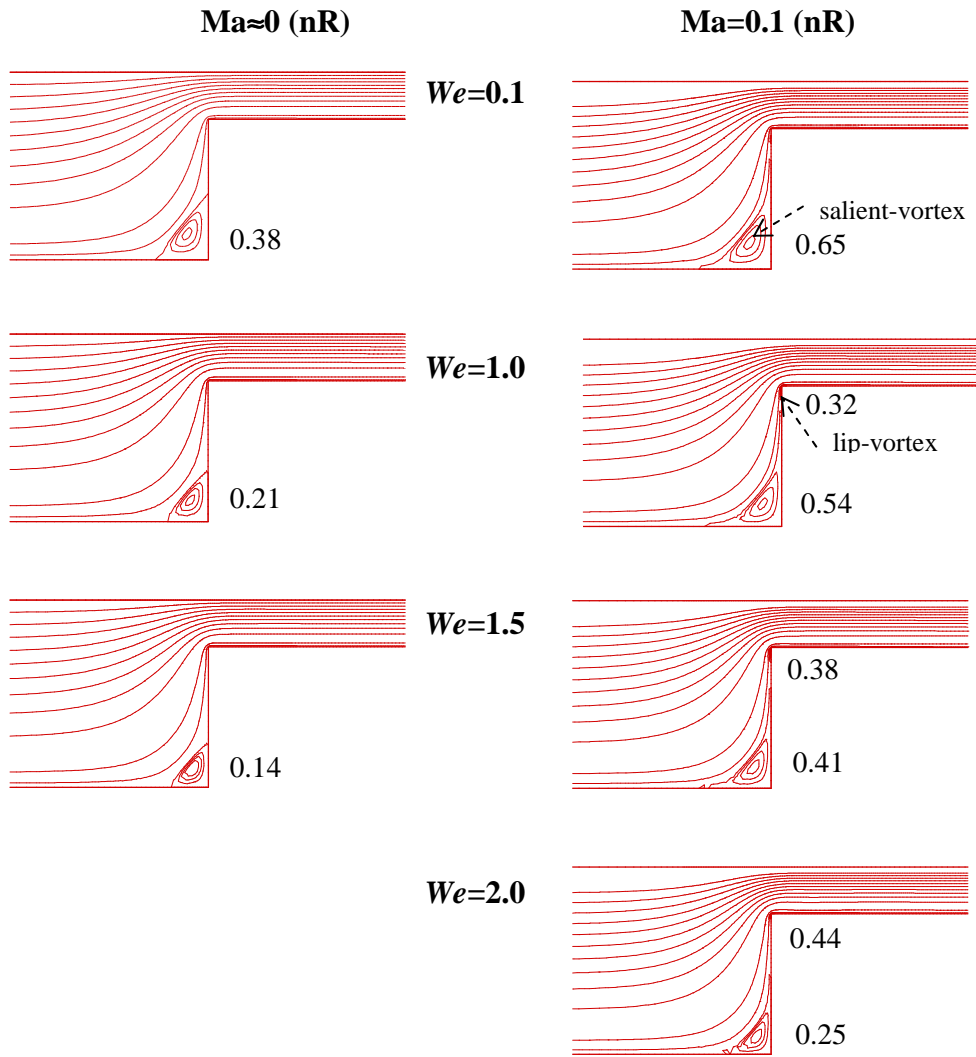


Figure 15. Streamline contours, increasing We : (left) incompressible and (right) compressible; inertial flows, fe scheme, vortex intensity $\times 10^{-3}$.

Table 1. Critical We level for different scheme variants and flow configurations.

	Re=0.0								Re=1.0	
	incompressible				compressible				compressible	
	fe		fe/fv		fe		fe/fv		fe	
	nR	R	nR	R	Ma≈0	Ma=0.1	Ma≈0	Ma=0.1	Ma≈0	Ma=0.1
Critical We	2.2	2.8	3.0	3.5	1.5	1.7	3.3	3.1	1.5	2.0
Peak N_1	73.7	79.1	105.9	85.1	53.3	54.4	194.0	200.8	51.1	68.6